Biophysical Journal
Article

Biophysical Society

Segmentation of 3D Trajectories Acquired by TSUNAMI Microscope: An Application to EGFR Trafficking

Yen-Liang Liu,[1] Evan P. Perillo,[1] Cong Liu,[1] Peter Yu,[1] Chao-Kai Chou,[2,3] Mien-Chie Hung,[2,3] Andrew K. Dunn,[1] and Hsin-Chih Yeh[1,*]

[1]Department of Biomedical Engineering, University of Texas at Austin, Austin, Texas; [2]Department of Molecular and Cellular Oncology, University of Texas MD Anderson Cancer Center, Houston, Texas; and [3]Center for Molecular Medicine and Graduate Institute of Cancer Biology, China Medical University, Taichung, Taiwan

ABSTRACT Whereas important discoveries made by single-particle tracking have changed our view of the plasma membrane organization and motor protein dynamics in the past three decades, experimental studies of intracellular processes using single-particle tracking are rather scarce because of the lack of three-dimensional (3D) tracking capacity. In this study we use a newly developed 3D single-particle tracking method termed TSUNAMI (Tracking of Single particles Using Nonlinear And Multiplexed Illumination) to investigate epidermal growth factor receptor (EGFR) trafficking dynamics in live cells at 16/43 nm (*xy*/*z*) spatial resolution, with track duration ranging from 2 to 10 min and vertical tracking depth up to tens of microns. To analyze the long 3D trajectories generated by the TSUNAMI microscope, we developed a trajectory analysis algorithm, which reaches 81% segment classification accuracy in control experiments (termed simulated movement experiments). When analyzing 95 EGF-stimulated EGFR trajectories acquired in live skin cancer cells, we find that these trajectories can be separated into three groups—immobilization (24.2%), membrane diffusion only (51.6%), and transport from membrane to cytoplasm (24.2%). When EGFRs are membrane-bound, they show an interchange of Brownian diffusion and confined diffusion. When EGFRs are internalized, transitions from confined diffusion to directed diffusion and from directed diffusion back to confined diffusion are clearly seen. This observation agrees well with the model of clathrin-mediated endocytosis.

INTRODUCTION

Single-molecule detection in aqueous solution has advanced our knowledge in molecular and cellular biology since its introduction in early 1990s (1–3). Whereas single-molecule imaging has led to the development of pointillism microscopy (4), such as PALM (5,6) and STORM (7), complex molecular trafficking and interaction dynamics inside live cells often cannot be deciphered by pointillism microscopy because of its limited temporal resolution (8). For nearly four decades, cellular dynamic processes have been probed using two ensemble and time-averaging techniques—fluorescence recovery after photobleaching (FRAP (9)) and fluorescence correlation spectroscopy (FCS (10)). Although FRAP and FCS provide sufficient temporal resolution (submilliseconds) to monitor fast molecular dynamic processes, their spatial resolution is limited by diffraction (11). Alternatively, rapid molecular dynamics can be studied at high spatial resolution using single-particle tracking (SPT (11–19)). Whereas SPT has made important discoveries that change our view of plasma membrane organization (17,19) and molecular motor dynamics (20), the use of SPT in monitoring "intracellular" processes is rather limited because of the lack of three-dimensional (3D) tracking capacity that can follow a single particle inside a live cell for a long period of time. In the past decade, new SPT techniques have been developed to visualize molecular motion in the 3D space (termed 3D-SPT), including multiple imaging planes (21,22), orbital tracking (23–25), point spread function engineering (26,27), and confocal tracking (28,29). Although allowing for direct observation of transport processes from membrane to cytoplasm, current 3D-SPT methods often suffer from shallow imaging depth (because of the use of one-photon excitation) and limited *z*-tracking range (e.g., astigmatism-based, nonfeedback tracking systems (27)), which prevent these methods from tracking single molecules inside multicellular models such as spheroids (see our review in (8)).

Submitted May 31, 2016, and accepted for publication September 26, 2016.

*Correspondence: tim.yeh@austin.utexas.edu

Editor: Julie Biteen

http://dx.doi.org/10.1016/j.bpj.2016.09.041

Our group has recently developed a new, to our knowledge, 3D-SPT method termed TSUNAMI (Tracking of Single particles Using Nonlinear And Multiplexed Illumination) that enables high-resolution tracking of single epidermal growth factor receptor (EGFR) complexes in live cancer spheroids (~100 μm thick), with track duration up to 10 min and vertical tracking depth up to tens of microns (30–33). As a wealth of information about membrane structure, interior organization, and receptor biology can be derived from the long 3D trajectories acquired by TSUNAMI, a sophisticated tool is needed to segment and classify these trajectories according to their motional modes (34–37), extract physical parameters of the motion (30,38), and correlate that motion to the surrounding environment (39), all with the goal of understanding the physical scenarios behind the observed motion (40,41). Considerable effort has been devoted to the identification of change points in motion (36) or diffusivity (38) along the same trajectory and to the visualization of spatial regions with different dynamic behaviors (34,35,38,42). Such an analysis is called trajectory segmentation and classification (11), which is often carried out by calculating a number of classification parameters over the trajectory using methods such as rolling window analysis (34,36,43), supervised segmentation (44), mean-squared-displacement (MSD) curvature (34,35,45,46), maximum likelihood estimator (38), Bayesian methods (47,48), F-statistics (49), hidden Markov model (50,51), and wavelet analysis (42,52).

In this study, we demonstrate an integrated trajectory analysis tool that adopts a combination of analytical strategies (34–37,39) and classification parameters (MSD scaling exponent (53–56), directional persistence (36,57), and confinement index (37,58)) in achieving effective segmentation and classification of both simulated and real-world trajectories. Our algorithm has achieved 81% accuracy in classifying segments along simulated 3D trajectories. From visual inspection, we find most of the misidentified segments near the change points of different motional modes. When analyzing 95 EGF-stimulated EGFR trajectories acquired in live skin cancer cells, we find that these trajectories can be separated into three groups—immobilization (24.2%), membrane diffusion only (51.6%), and transport from membrane to cytoplasm (24.2%). When EGFRs are membrane-bound, they show an interchange of Brownian diffusion and confined diffusion. When EGFRs are internalized, transitions from confined diffusion to directed diffusion and from directed diffusion back to confined diffusion are clearly seen. As expected, the speed observed in the directed diffusion matches well with the speed of the typical molecular motor-mediated transport (0.5–2 μm/s) (59–62). When compared with the stimulated EGFRs, the untreated EGFRs clearly show increased mobility on membrane. Reduced mobility for stimulated EGFRs is likely due to EGFR dimerization (50,63), which induces endocytosis (64).

MATERIALS AND METHODS

TSUNAMI tracking microscope

TSUNAMI is a feedback-control tracking system that employs a spatiotemporally multiplexed two-photon excitation and temporally demultiplexed detection scheme (Figs. S1 and S2 in the Supporting Material). Submillisecond temporal resolution (under high signal-to-noise conditions) and subdiffraction tracking precision in all three dimensions have been previously demonstrated (30). Tracking can be performed at depths up to 200 μm in highly scattering environments (30,31).

Excitation of 835 nm from a Ti:Al_2O_3 laser (Mira 900, Coherent, Santa Clara, CA) is used for tracking experiments. Following the optical multiplexer, the beams pass through a galvo scanning system (6125H, Cambridge Technology, Bedford, MA), before being focused through a 60 × N.A. 1.3 silicone oil objective (UPLSAPO 60X, Olympus, Center Valley, PA). The total laser power was ~8mW at the objective back aperture. For a typical 40 nm red fluorescent bead (F8770, Thermo Fisher Scientific, Waltham, MA), photon count rates were in the range of 200–500 kHz. Background fluorescence signal was on the order of 3 kHz that includes a 150 Hz background signal from the detector. Signal-to-noise ratios were typically above 20. Demultiplexed detection is performed electronically via time-correlated single-photon counting (TCSPC) analysis. Fluorescence signals are detected by a cooled GaAsP photomultiplier tube with 5 mm square active area (H7422PA-40, Hamamatsu, Bridgewater, NJ) in nondescanned configuration. The current output from the PMT is amplified through a 2 GHz cutoff bandwidth preamplifier (HFAC-26, Becker and Hickl, Berlin, Germany) and sent into a photon-counting board (SPC-150, Becker and Hickl, Berlin, Germany) to be counted and correlated to the 76 MHz reference clock of the laser oscillator. The instrument response function (IRF) is measured to be 230 ps FWHM. Every 1–20 ms a photon histogram is sampled from the TCSPC module and processed in the software loop run in LabVIEW (National Instruments, Austin, TX). The tracking algorithm employs a proportional control to convert the error signals to new stage positions. New voltages are sent out through a DAQ card (PCIe-6353, National Instruments, Austin, TX) to their respective actuators—galvo mirrors for x and y tracking and piezo objective stage for z tracking. The saved voltages are converted to build a 3D tracking trajectory.

Trajectory segmentation and classification

We have developed a procedure to perform trajectory segmentation and classification (Fig. 1). First, a temporal rolling window of length w centered at time s on the trajectory (34,36) is adopted for calculating the segmented MSD at s ($MSD_{w,s}$, Fig. 1 *A*). As the motional mode of the tracked particle can vary significantly from one segment to another, a wide distribution of the segmented MSD curves is expected. We then perform a two-step test (Fig. 1 *B*) to classify the motion of each segment into four modes: 1) directed diffusion, 2) Brownian diffusion, 3) confined diffusion, and 4) immobilization. Within each segment only one of these motional modes is assigned.

The first step of the test is to differentiate directed motion (active transport) from Brownian diffusion, confined diffusion, and transient immobilization (passive motion) by evaluating two parameters from the segmented trajectories and their derived MSD curves—scaling exponent (α) (34) and directional persistence ($\Delta\phi$) (36). By fitting each segmented MSD curve with the following power-law equation (41), a single α value is obtained and is assigned to each time point s along the trajectory as follows:

$$\mathrm{MSD}(t) \sim t^{\alpha}. \quad (1)$$

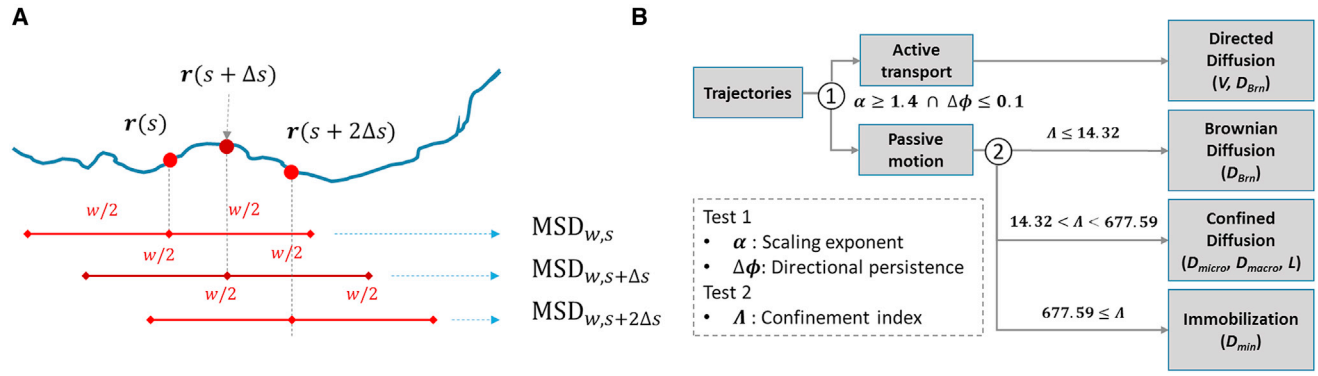

FIGURE 1 Procedure for segmentation and classification of trajectories. (*A*) The rolling window analysis is conducted at a given time point s with the length of rolling window of 1.6 s ($w = 1.6$ s) and the sliding time step (Δs) of 0.1 s. (*B*) The transient behaviors of a trajectory are identified using the three classification parameters: scaling exponent of MSD curve (α), directional persistence ($\Delta\phi$), and confinement index (Λ). The MSD curve of each segment is fitted with the proper model to extract the dynamic parameters including V, D_{Brn}, D_{micro}, D_{macro}, L, and D_{min}. To see this figure in color, go online.

Directional persistence function ($\Delta\phi$) in a temporal rolling window of length w centered at time s is defined as (36) follows:

$$\Delta\phi(t) = \left\langle \left(\phi(t'+t) - \phi(t')\right)^2 \right\rangle^{\frac{1}{2}},\ t' \in \left[s - \frac{w}{2}, s + \frac{w}{2}\right], \quad (2)$$

where ϕ is the directional vector at each data point (see Fig. S3 *B*). Although, each rolling window centered at s generates a directional persistence function $\Delta\phi(t)$, we use the single value, $\Delta\phi(w/4)$, to represent the direction persistence $\Delta\phi$ at s. The time lag of $w/4$ is chosen in consideration of the microtubule bending during a motor-driven event (36). The $\Delta\phi$ is equal to zero when the motion is unidirectional. Similar angle analysis (e.g., jump angle analysis) is used to probe diffusion bias inside nucleus (65,66).

The segment at time s is classified as active transport when $\alpha \geq 1.4$ and $\Delta\phi \leq 0.1$ (test 1 in Fig. 1 *B*). Otherwise the segment is classified as passive motion (threshold optimization is discussed in the Supporting Material and Fig. S4). In the complex intracellular environment, the active transport along microtubules has α values ranging from 1.4 to 2 (53). Whereas some biological studies also used the α value of 1.4 as a criterion for classification (54,55), an α value of 1.7 was used in a microfluidic experiment (36). In the same report, the criterion of $\Delta\phi \leq 0.1$ was found suitable to achieve sufficient discrimination between active and passive motion (36). The threshold values of α and $\Delta\phi$ have also been validated in our simulated movement experiment (SME; see the detailed discussion on SME below).

The second step of test is to classify passive motion into Brownian diffusion, confined diffusion, and immobilization by evaluating confinement index (Λ) from the segmented trajectories (test 2 in Fig. 1 *B*). Confinement index (Λ) is defined as (37,58) follows:

$$\Lambda = \frac{D_{max} w}{var(r)}, \quad (3)$$

where D_{max} is the unconstrained diffusivity of particles and $var(r)$ stands for the variance of particle positions (r) within a temporal rolling window of length w. In the early reports, confinement index is defined as the ratio of D_{max} w and r^2_{max}, where r_{max} is the largest displacement from the starting point within the rolling window (43). Under Brownian diffusion, r^2_{max} scales linearly with $D_{max}w$. But when the particle is confined in a domain of linear size L, r^2_{max} is limited by L^2. Thus the value of Λ becomes significantly larger than that in Brownian diffusion. In Eq. 3, r^2_{max} is replaced with $var(r)$ in the Λ calculation. As a result, Λ becomes the ratio of the variance of Brownian diffusion ($D_{max}w$) and the variance of trajectory segmented under study ($var(r)$). This modified definition of Λ has advantage in detecting confinement in a wider class of trapping potential shapes (37). Two threshold values were selected: $\Lambda_{Brn} = 14.32$ and $\Lambda_{Im} = 677.59$. Based on these thresholds, trajectories were classified into Brownian diffusion ($\Lambda \leq \Lambda_{Brn}$), confined diffusion ($\Lambda_{Brn} < \Lambda < \Lambda_{Im}$), and immobilization ($\Lambda \geq \Lambda_{Im}$). Threshold optimization is discussed in Discussion (also see Fig. S5).

For trajectory segmentation and classification, the length of temporal rolling window (w) should be sufficiently long to ensure good estimation of α, $\Delta\phi$, and Λ (36). On the other hand, the w should be kept short to maintain decent temporal resolution. Optimization of rolling window length is discussed in the Supporting Material (Fig. S4). We found that the reasonably short rolling window of 1.6 s (w) can effectively differentiate active transport from passive motion (Fig. S4) and distinguish confined diffusion from Brownian diffusion (Fig. S5). The sliding time step (Δs) for the rolling window analysis is set as 0.1 s, whereas the time step for position acquisition (Δt) is either 2.5 ms for simulated trajectories or 20 ms for experimental trajectories. In our simulations, we also found that the confinement index of Brownian motion is independent of the rolling window length (w), but the scaling exponent (α) of directed diffusion, the directional persistence ($\Delta\phi$) of directed diffusion, and the confined index (Λ) of confined diffusion are all functions of the rolling window length (Figs. S4 and S5).

Extracting dynamic parameters from MSD

The typical approach to analyze a single-particle trajectory starts with the calculation of MSD, which describes the average squared distance (r^2) that the particle has explored in space at a given time lag (t) (see Fig. S3 *A*). Because the cellular environment is highly crowded with a compartmentalized structure, the dynamics for receptors, even of the same type, can be highly heterogeneous (67). Observed motion in a live cell can be comprised of periods of Brownian diffusion, directed diffusion, confined diffusion, and transient immobilization, all within an individual receptor trajectory. For Brownian diffusion, the MSD can be calculated as the variance of the solution to the Fick's law of diffusion and it scales linearly with t as follows:

$$\mathrm{MSD}(t) = \left\langle \left(\boldsymbol{r}(t'+t) - \boldsymbol{r}(t')\right)^2 \right\rangle = 2dD_{Brn}t, \quad (4)$$

where d represents the dimensionality of the space in which the motion takes place, D_{Brn} is the Brownian diffusion coefficient, and r is the position vector of the particle.

Directed diffusion corresponds to the superposition of a ballistic movement and Brownian diffusion. It is characterized by the following quadratic scaling relationship (68):

$$\mathrm{MSD}(t) = 2dD_{lateral}t + (Vt)^2, \quad (5)$$

where V represents the speed of the ballistic movement that is most likely caused by molecular motor-assisted active transport along microtubules. As Brownian diffusion is most noticeable in the lateral direction of ballistic movement, $D_{lateral}$ is used to represent it.

Confined diffusion, the constrained particle diffusion due to receptors being trapped in small cellular compartments such as cortical cytoskeleton, membrane cavities, and vesicles (37), is featured by an abrupt change of slope in the MSD curve (35) after a characteristic equilibration time τ (see Fig. S8 for discussion on various types of confined diffusion). Although the exact expression of MSD depends on the shape of the confining region and on spatial dimensionality, the two-dimensional (2D) MSD of confined diffusion can be approximated by (39,69)

$$\mathrm{MSD}_{2D}(t) \cong \frac{L^2}{3}\left[1 - \exp\left(-\frac{t}{\tau}\right)\right] + 4D_{macro}t, \qquad (6)$$

where D_{macro} is the long-term "macroscopic" diffusion coefficient (69) and L is the linear dimension of the confinement. The characteristic equilibration time τ can be related to L by the following (39):

$$\tau = \frac{L^2}{12(D_{micro} - D_{macro})}, \qquad (7)$$

where D_{micro} is the short-term "microscopic" diffusion coefficient (39,69). This intradomain diffusivity D_{micro} is measured using the same method as described in Brownian diffusion section.

Transient immobilization takes place when the diffusivity falls below a predefined value D_{min} (1.9×10^{-4} $\mu m^2/s$), which is the detection limit of our TSUNAMI microscope (see Fig. S6 for detailed discussion).

MSD curve fitting

Curve fitting of segmented MSD using Eqs. 4–6 can extract local dynamic parameters such as Brownian diffusion coefficient (D_{Brn} and $D_{lateral}$), active transport speed (V), linear dimension of compartments (L), macroscopic diffusivity (D_{macro}), and microscopic diffusivity (D_{micro}). For each segment classified as Brownian diffusion, the associated D_{Brn} is optimally determined using a covariance-based estimator (70). Here we define the instantaneous diffusivity (D_0) as the linear MSD fitting result of each rolling window (regardless the classification result of that rolling window). Since MSD at a longer time lag is averaged over fewer samples (i.e., noisier), typically only the first 1–20 data points in the MSD curve are used for diffusivity estimation in a short time period (35,69,71–73). The optimal number of data points used for D_0 estimation should be determined by expected diffusion coefficient, tracking error, size of time step, and track duration. Considering these factors in our experiments, we estimate D_0 based on the first 3–5 points in the MSD curve. The detection limit of the TSUNAMI microscope is currently at 1.9×10^{-4} $\mu m^2/s$ (D_{min}, Fig. S6).

Following the definition of D_0, we define the instantaneous velocity (V_i) as the absolute displacement within a rolling window divided by the length of that rolling window, regardless of the classification result of that rolling window. In this report, D_{Brn} and V are the dynamic parameters derived from the segments classified as Brownian and directed diffusion, respectively, whereas D_o and V_i are the parameters derived from all segments regardless their classification results. Readers are advised to pay attention to these different notations and their associated definitions.

For segments classified as directed diffusion or confined diffusion, a least squares regression line is fitted through the first N_f points of the MSD curve with each point weighted by the reciprocal of its relative variance var_{rel} (68):

$$var_{rel}(t) = \frac{t(2t^2 + 1)}{w - t + 1}, \qquad (8)$$

where w is the length of rolling window and t is the time lag of MSD curve. The values of N_f are typically $N/3$ ($N_f = 16$) (74), $N/2$ ($N_f = 28$) (75), and $2N/3$ ($N_f = 50$), where N is the number of total MSD data points (34). As a precise measure of the dynamic parameters requires a sufficient number of MSD points, we choose $N_f = 40$ ($N/2$, $N = 80$ ($w = 1.6$ s and $\Delta t = 20$ ms)) in calculating the dynamics parameters of directed and confined diffusion.

Verifying 3D tracking and trajectory analysis algorithm using SME

The accuracy of dynamic parameters extracted from MSD curves is limited by the tracking error of our system. To precisely quantify the tracking error of TSUNAMI microscope, we tracked a fixed fluorescent bead (200 nm, F-8810, Thermo Fisher Scientific) loaded on an independent xyz piezo stage (P-733K130, Physik Instrumente (PI), Karlsruhe, Germany), which is programmed to carry out motion patterns generated by Monte Carlo simulation. This control experiment is termed the SME (Fig. S1) and the simulation-generated trajectory is termed the prescribed trajectory. To characterize the tracking error in a scattering environment, fluorescent beads were embedded in 1.3% agarose within chambered coverglasses. We neglected the finite differences between the Monte-Carlo-simulation-generated trajectory (that was used to command the movement of the xyz piezo stage) and the trajectory that the stage actually performed (determined by the capacitive sensors of the stage). The tracking error of TSUNAMI microscope is defined as the standard deviation of the differences between the stage trajectory and the TSUNAMI tracking trajectory. The tracking error was found less than 20 nm in x and y and ranged from 51–91 nm in z, depending on the diffusivities used in the SME (Fig. S9). In a prescribed motion that mimicked the typical 2D confined diffusion of membrane receptors, the TSUNAMI tracking error was found to be 16 nm in xy and 43 nm in z (Fig. S10). Tracking error can also be caused by the thermomechanical instability of the microscope (69). For 100 s tracking experiments, the static error is found significantly smaller than the dynamic error (Fig. S6).

Cell culture

Used as the model system, EGFR-overexpressed A431 skin cancer cell was purchased from ATCC and grown in DMEM (Dulbecco's Modified Eagle Medium, 11995-065, Thermo Fisher Scientific) supplemented with 10% fetal bovine serum (16140-071, Thermo Fisher Scientific). The cell cultures were kept in humidified atmosphere with 5% CO_2 at 37°C. Single suspensions were prepared by mild enzymatic dissociation using a 0.25% trypsin/EDTA solution (25200-056, Thermo Fisher Scientific). For EGFR tracking in monolayer cells, A431 cells were seeded onto optical imaging eight-well chambered coverglasses (154534, Thermo Fisher Scientific) with cell density of 1×10^5 cells per well and allowed to adhere overnight.

Multicellular spheroid preparation

Agarose-coated 96-well plates (130188, Thermo Fisher Scientific) were used to cultivate A431 spheroids. Agarose coating was conducted by filling each well with 50 μL DMEM sterilized agarose solution (1.5% by weight, A9539-100G, Sigma-Aldrich). The spheroids were prepared following the procedure described in literature (76) and the plates were incubated for 96 h in humidified atmosphere with 5% CO_2 at 37°C. To generate spheroids with various sizes, single-cell suspensions from liquid overlay culture were seeded onto agarose-coated plates at different cell densities: 125, 250, 500, 1000, 1500, 2000, and 3000 cells per well (Fig. S15). Considering the penetration depth of the cell membrane dye (CellMask Deep Red, C10046, Thermo Fisher Scientific) and the working distance of the

objective, spheroids with diameters of 90 to 110 μm (seeding density ~125 cells per well) were selected for the tracking experiments.

Fluorescent probe labeling to EGFRs

Anti-EGFR antibody-conjugated fluorescent nanoparticles were used to label EGFRs for tracking. Biotinylated monoclonal anti-EGFR IgG (Ab-3, MS-311-B, Thermo Fisher Scientific) was mixed at 1:1 ratio with 40 nm red fluorescent nanoparticles (F8770, Thermo Fisher Scientific) in 1.5% BSA/phosphate-buffered saline solution (BSA, S7806, Sigma-Aldrich). The antibody-conjugated fluorescence nanoparticles (~30 nM, the stock solution) can be stored at 4°C for up to 1 week. The number of antibodies per nanoparticle should follow a Poisson distribution (77). In our experiments, we cannot rule out the possibility of cross-linking due to conjugating multiple antibodies on a single nanoparticle. The brightness of an antibody-conjugated fluorescent nanoparticle was characterized by fluorescence correlation spectroscopy and tracking of fixed particles (Fig. S16).

Before tracking experiments, both monolayer cells and spheroids were kept under serum-starvation conditions for 24 h. For monolayer samples, cells were stained with CellMask Deep Red (1:1000 dilution in DMEM) for 10 min at 37°C. For spheroid samples, spheroids were transferred from a 96-well plate to an 8-well chambered coverglass using micropipette (8 to 10 spheroids per well). To ensure thorough membrane staining, a higher concentration of CellMask Deep Red (1:500 dilution) and a longer incubation time (1 h) were employed. After membrane staining, the staining buffer was replaced with the EGFR-labeling solution (antibody-conjugated fluorescent nanoparticles at 100 pM) diluted from the stock solution (30 nM). The reaction was incubated for 30 min at 37°C (preparation steps are graphically presented in Fig. S17). The EGFR-labeling solution was removed, and the samples were washed twice using phosphate-buffered saline to remove the unbound fluorescent nanoparticles. Under these conditions, each A431 cell was expected to have 3–8 EGFRs labeled with a single fluorescent bead. At such a low labeling density, the chance for one fluorescent bead to encounter another bead or to crosslink multiple EGFRs was minimal. Without anti-EGFR antibodies in reaction, very few fluorescent beads (typically aggregates) were found on the cell membrane (<0.27 bead/cell) (Fig. S18).

Upon completion of membrane staining and EGFR labeling, the chambered coverglass was immediately put on the TSUNAMI microscope for tracking experiments. Internalization of EGFR was initiated by replacing the media with DMEM containing 10 ng/ml EGF (recombinant human epidermal growth factor, PHG0311L, Thermo Fisher Scientific) (64). As membrane-bound EGFRs were typically internalized within 30 min upon EGF stimulation (78), 2–4 EGFR trajectories (duration ranged from 2–10 min) were typically obtained from each well. The volumes of all solutions and washing buffers used in staining were 200 μl per well.

RESULTS

Verifying 3D tracking and trajectory analysis algorithm using SME

The reliability of the TSUNAMI 3D tracking microscope and the trajectory analysis algorithm was verified by following prescribed trajectories that imitated EGFR trafficking in live cells. One 35 s representative prescribed trajectory (Fig. 2) was divided into seven 5-s-long regions, where three were encoded with confined diffusion (*green areas*), two were encoded with Brownian diffusion (*blue*), one was encoded with directed diffusion (*red*), and the last one was encoded with immobilization (*gray*). In our trajectory analysis, every 0.1-s-long segment was classified into one of the four motional modes (the sliding time step (Δs) was 0.1 s, Fig. 1) and color-coded for visual inspection. It is obvious to see that one classification parameter alone could not well identify the motional modes (Fig. 2 *B*). In this example, our algorithm successfully recovered the seven regions and reached 81% overall segment classification accuracy.

The misclassified segments concentrated near the change points between regions. In particular, misidentification of confined diffusion as Brownian diffusion took place when the motion changed from confined diffusion (*green*, 10–15 s) to directed diffusion (*red*, 15–20 s). Similarly, when motion changed from Brownian diffusion (*blue*, 25–30 s) to immobilization (*gray*, 30–35 s), misclassification of immobilization as confined diffusion was also noticed. These systematic misidentifications around the change points were understandable as the classification parameters were averaged over a 1.6-s-long rolling window (w), which could span two or more distinctive motion modes. Because of these misclassifications, the experimentally derived dynamic parameters often needed to be fitted with a Gaussian mixture model (MATLAB, The MathWorks, Natick, MA). For the directed diffusion region (*red areas* in Fig. 2 *B*), the predetermined active transport speed (V_{pre}) and the experimentally recovered active transport speed (V) were 2 μm/s and 2.05 $\pm$ 0.06 μm/s, respectively (where the error was the standard deviation of the Gaussian fit, Fig. 2 *D*). Here the 2.05 $\pm$ 0.06 μm/s was the major population, whereas the overall population (considering the presence of subpopulation) was calculated to be 1.96 $\pm$ 0.28 μm/s. For the Brownian diffusion regions (*blue areas*), the predetermined diffusivity (D_{pre}) and the experimentally recovered diffusivity (D_{Brn}) were 0.08 μm^2/s and 0.05 $\pm$ 0.02 μm^2/s, respectively (whereas the overall population to be 0.04 $\pm$ 0.03 μm^2/s). For the confined diffusion regions (*green areas*), the predetermined confinement size (L_{pre}) and the experimentally recovered confinement size (L_{exp}) were 100 nm and 100.1 $\pm$ 46.2 nm, respectively (whereas the overall population to be 131.1 $\pm$ 84.2 nm). More SME results that demonstrate the reliability of the trajectory analysis algorithm can be found in Figs. S11–S13.

Revealing membrane dynamics of EGFRs

We used the developed algorithm to analyze 112 EGFR trajectories acquired in live A431 epidermoid carcinoma cells (95 with stimulation of EGFs and 17 without stimulation). These trajectories all started on the apical surfaces of the cells, and consequently were expected to exhibit an interchange of confined diffusion and Brownian diffusion at the beginning (16). One representative 120-s-long

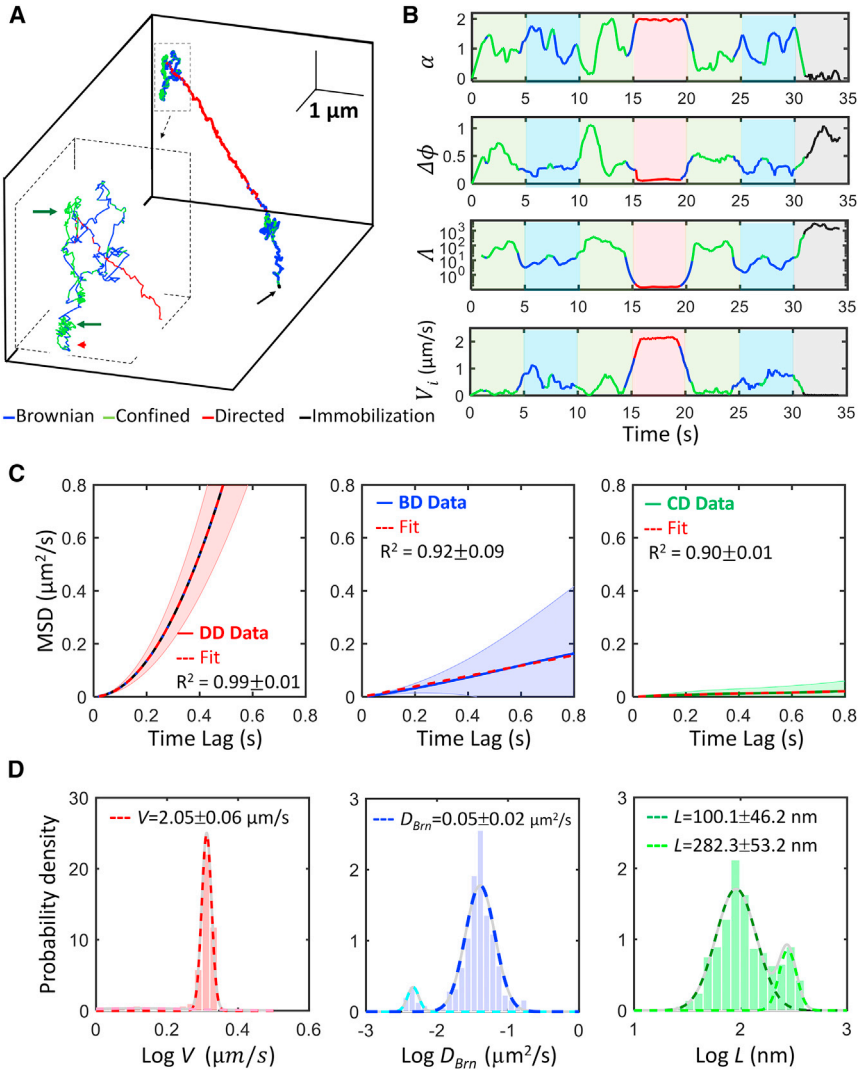

FIGURE 2 Verifying the trajectory analysis algorithm using SME system ($n = 16$). (*A*) A representative prescribed trajectory is composed of Brownian diffusion (BD), confined diffusion (CD), directed diffusion (DD), and immobilization (IM). Simulated conditions are Brownian diffusivity $D_{pre} = 0.08\ \mu m^2/s$, linear dimension of the confinement $L_{pre} = 100$ nm, probability of penetration $P = 0.01$, and speed of directed diffusion $V_{pre} = 2\ \mu m/s$. The track duration is 35 s, and the trajectory is equally divided into seven 5-s-long regions in which the tracked particle exhibits four types of motional modes in the following sequence: CD→BD→CD→DD→CD→BD→IM. The red arrowhead marks the starting point of the trajectory. The green arrows mark the regions exhibiting confined diffusion and the black arrow marks the immobilization region. (*B*) Time traces of the three classification parameters (α, $\Delta\phi$, Λ) and instantaneous velocity (V_i) of the representative trajectory shown in (*A*). (*C*) The ensemble-averaged MSD curves from the classified regions were fitted with the proper models to recover the dynamic parameters (D_{Brn}, L, and V). The R-squared values were employed to evaluate the goodness-of-fit. Ribbons represent the standard deviations. (*D*) Normalized histograms of experimentally derived dynamic parameters log$V$ (*red*), logD_{Brn} (*blue*), and log$L$ (*green*) are provided. The means and standard deviations were from curve fitting with a Gaussian mixture model. The total number of trajectories analyzed is 16 in (*C*) and (*D*). To see this figure in color, go online.

trajectory clearly showed these two motional modes on the cell membrane, with the fractions of confined time and free-diffusing time being 85% and 15%, respectively (Fig. 3). For Brownian diffusion segments (*blue*), the measured diffusivity, D_{Brn}, was $(3.2 \pm 0.5) \times 10^{-3}\ \mu m^2/s$. For confined diffusion, the measured diffusivities, D_{micro} and D_{macro}, were $(3.3 \pm 0.6) \times 10^{-3}\ \mu m^2/s$ and $(0.5 \pm 0.7) \times 10^{-3}\ \mu m^2/s$, respectively. The linear dimension of confinement, L, was found to have two distributions: 48.8 ± 13.9 nm and 110.5 ± 85.8 nm (Fig. 3 *D*). These values agree with previous observation of membrane-bound EGFR dynamics using 2D single-particle tracking techniques (50,58).

Monitoring EGFR trafficking from membrane to cytoplasm in live cells

TSUNAMI is one of the few high-spatiotemporal-resolution 3D tracking techniques (8,23,25,79,80) that allow for monitoring intracellular processes and generating 3D trajectories over a large z depth (>30 μm) and a long period of time (~10 min). One representative 442-s-long trajectory clearly exhibited features of EGFR trafficking from membrane to cytoplasm (Fig. 4 *A*). After the trajectory was segmented, classified, and color-coded, four different phases could be clearly identified: confined diffusion on the cell membrane (phase I), onset of the internalization process (phase II), active intracellular transport (phase III), and confined diffusion in a vesicle (phase IV). The durations of these four phases were 177, 124, 10, and 131 s, respectively (Fig. 4 *B*).

Phase I was featured by high confinement indices (average $\Lambda = 45.6 \pm 22.8$) and very small displacements within 20 ms (average absolute displacement = 13.3 ± 6.5 nm per 20 ms), indicating confined diffusion on the cell membrane. As the cell membrane was stained with CellMask, we confirmed that the phase I trajectory was indeed on the cell membrane by superimposing the trajectory over the two-photon scanning image of the cell. Interestingly, we often observed EGFR

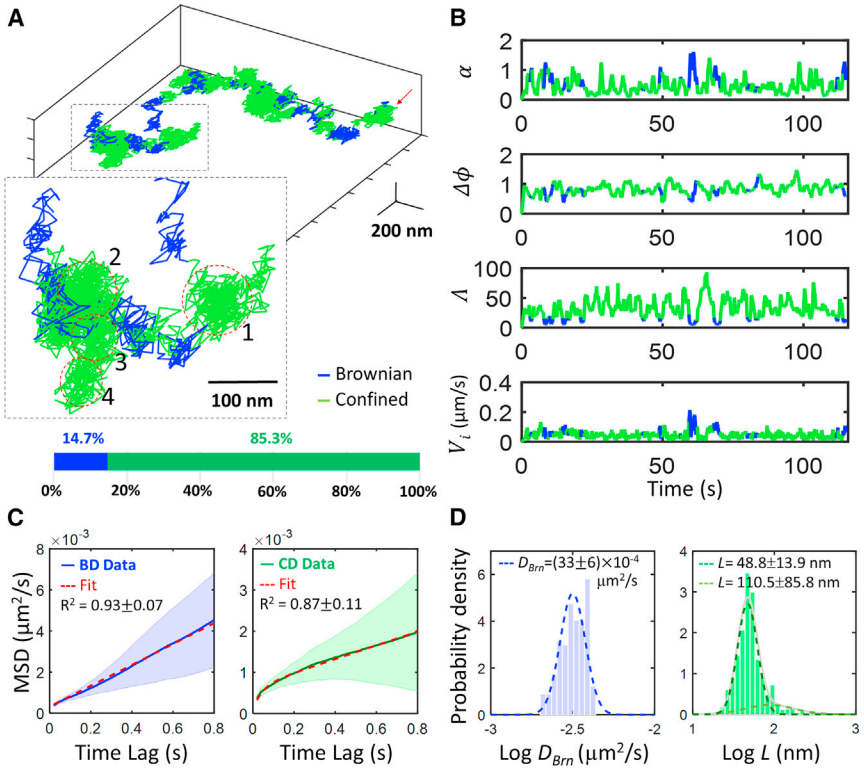

FIGURE 3 Interchanging of confined diffusion and Brownian diffusion on cell membrane. (*A*) A representative trajectory of EGFR membrane diffusion is shown. The green and blue colors represent confined diffusion and Brownian diffusion, respectively. The zoom-in view (*inset*) shows the membrane confinements based on visual inspection. The fractions of free diffusion time and confinement time were 14.7% and 85.3%, respectively. (*B*) Time traces of the three motion classification parameters (α, $\Delta\phi$, Λ) and instantaneous velocity (V_i) of the representative trajectory shown in (*A*) are provided. (*C*) The ensemble-averaged MSD curves from the classified segments were fitted with the proper models to extract D_{Brn} and L. The R-squared values were employed to evaluate the goodness-of-fit. Ribbons represent the standard deviations. (*D*) Histograms of logD_{Brn} and log$L$ derived from the classified segments are provided. These histograms were fitted with a Gaussian mixture model. To see this figure in color, go online.

movement toward one direction on membrane (Fig. 4, *C-I*). This type of the "linear" confined diffusion of transmembrane proteins has previously been reported by other groups (81), possibly reflecting diffusion within a linear confinement.

Phase II was featured by an interchange of Brownian and directed diffusion, which we believe marked the onset of the internalization. If internalization of EGFR is carried out by clathrin- and actin-mediated endocytosis, phase II should represent the pulling of clathrin-coated pits toward the interior of the cell by the movement of the growing actin network (82) and the formation of endosome mediated by dynamins (83). There was a noticeable peak in the instantaneous velocity (V_i) time trace in phase II, from 266 to 275 s (Fig. 4 *D*, *inset a*). The average V_i within this 9-s window was significantly higher than the background level (0.16 vs. 0.05 μm/s). This increased velocity agreed well with the clathrin-mediated endocytosis model as the internalization speed of clathrin-coated pits is found on the order of 0.1 μm/s (84). Upon a closer examination of the color-coded phase II trajectory (Fig. 4, *C-II*), a change point (*marked by a red arrow*) from the red-blue-mixing region to the green-blue-mixing region was clearly noted. We believe this change point marked the transition from the actin-cytoskeleton-mediated movement (*red-blue-mixing*) to the confined diffusion in an early endosome (*green-blue-mixing*).

A sudden increase of instantaneous velocity at 302 s marked the beginning of phase III, which was featured by a large linear displacement (8.17 μm in Fig. 4, *C-III*) within a short period of time (10 s). Phase III was believed to be the active transportation of endosome on microtubules (i.e., directed diffusion) (34,60). Both the average instantaneous velocity of 1.20 $\pm$ 1.06 μm/s (V_i) and the active transport speed of 1.39 $\pm$ 0.99 μm/s (V, from Eq. 5) derived from phase III matched well with the typical motor protein-mediated transport speed of 0.5 to 2 μm/s (59–62). The two separate populations of V_i in phase III might represent the two classes of runs (the short-slow run and the long-fast run) observed in active transport (85,86) (Fig. 4 *F*). The short-slow run represents motors engaged in a tug-of-war between oppositely directed molecular motors attached to the same cargo (87,88). The long-fast run (~4 μm displacement and ~3 s duration, such as the movement within 305 to 308 s in phase III, Fig. 4 *D*, *inset b*) indicates that dynein motors become dominate in the intracellular transportation. The length and duration of active transport of EGFRs (derived from the 95 EGF-stimulated EGFR trajectories) were 3.89 $\pm$ 1.69 μm and 5.05 $\pm$ 4.50 s, respectively.

The instantaneous velocity suddenly decreased to the background level at 311 s (~0.05 μm/s), which marked the end of active transportation and the beginning of phase IV. Featured by a mixture of confined and Brownian diffusion (Fig. 4 *C-IV*), phase IV was believed to be a diffusion confined within a vesicle (late

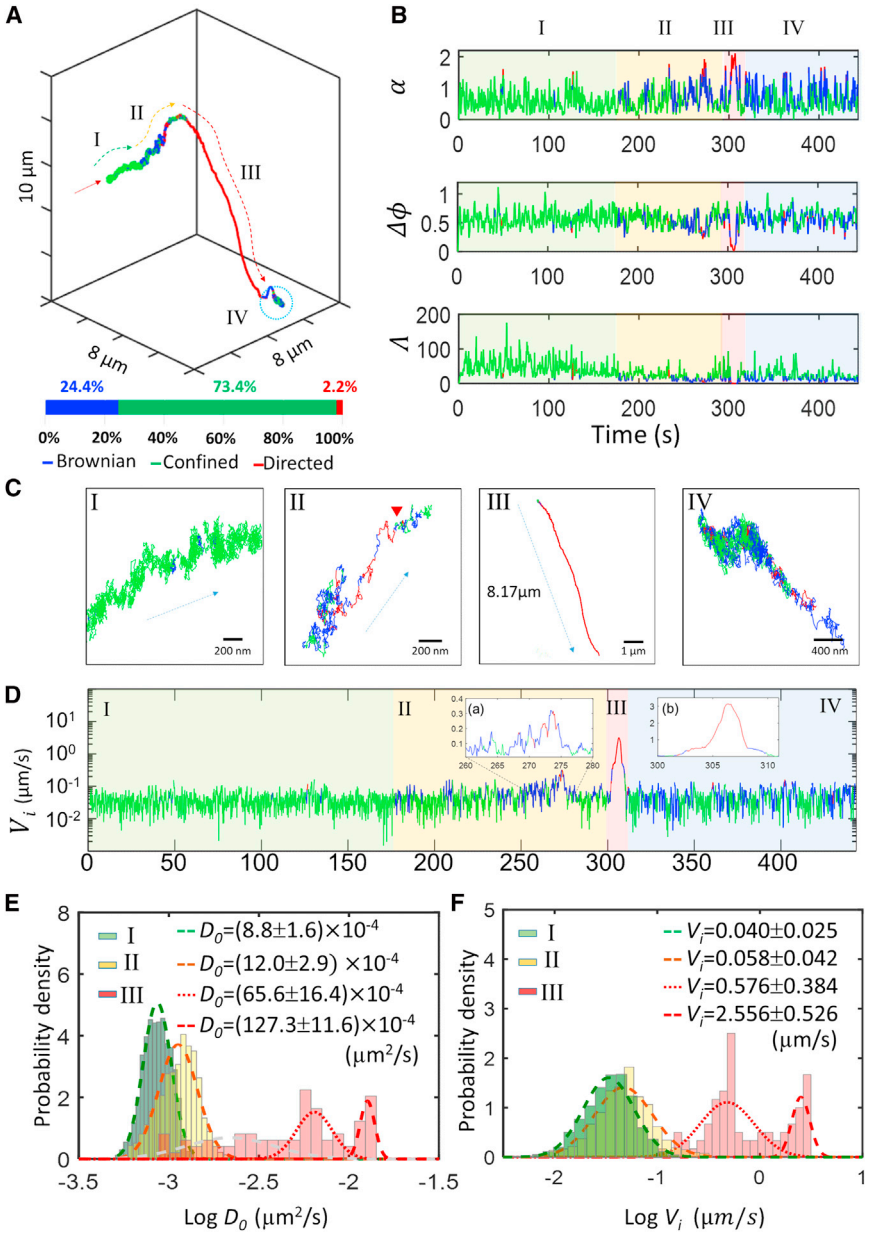

FIGURE 4 Trafficking from membrane to cytoplasm. (*A*) A representative trajectory of EGFR trafficking from cell membrane to cytoplasm is shown. The green, blue, and red colors represent confined, Brownian, and directed diffusion, respectively. The dark red arrow marks the starting point of the trajectory. The fractions of free diffusion time, confinement time, and active transport time were 24.4%, 73.4%, and 2.2%, respectively. The trajectory can be divided into four phases by visual inspection. (*B*) Time traces of the three motion classification parameters (α, $\Delta\phi$, Λ) is shown. Corresponding periods of the four phases are color-coded in these time traces. (*C*) Zoom-in views of the four phases, which clearly show the differences in the receptor motion in these phases. In this case, EGFR complex traveled 8.17 μm into the cytoplasm at phase III. (*D*) Time trace of instantaneous velocity (V_i) is shown. A small peak was noted around 273 s in phase II (*inset a*) and a large peak took place around 307 s in phase III (*inset b*), which mark the onset of internalization and the motor-mediated transport, respectively. (*E*) Histograms of logD_0 in phases I–III are provided. (*F*) Histograms of logV_i in phases I–III are provided. The values shown in (*E*) and (*F*) represent the means and standard deviations from Gaussian mixture model fitting. The logD_0 and logV_i of phase III clearly show two distributions. These two distributions are indicated with dotted line and dashed line, respectively. To see this figure in color, go online.

endosome) that itself diffused (69) (called cage diffusion in Fig. S8).

The histograms of logD_o were clearly distinguishable for phases I, II, and III (Fig. 4 *E*). The logD_o histogram of phase IV was similar to that of phase I and was thus not shown (Fig. S14). Similarly, the histograms of logV_i were also distinguishable for phases I, II, and III. Whereas logD_0 and logV_i of phases I and II had a normal distribution, those of phase III clearly had a much broader distribution. The average D_{Brn}, L, D_{micro}, D_{macro}, V_i, and V values for each phase are summarized in Table 1. For the entire trajectory (442 s long), the fractions of free diffusion time, confinement time, and active transport time were 24.4%, 73.4%, and 2.2%, respectively.

Distributions of the dynamic parameters of EGFR

Based on the classification results, the 95 EGF-stimulated EGFR trajectories were divided into three groups—group 1: stalled EGFRs (n = 23, 24.2%), group 2: membrane diffusing EGFRs (n = 49, 51.6%), and group 3: membrane to cytoplasm trafficking EGFRs (n = 23, 24.2%) (Fig. 5 *A* showing a representative trajectory in each group). Group 1 trajectories were characterized by either immobilization ($\Lambda \geq \Lambda_{Im}$) or confined diffusion within a region of linear size of 500 nm or smaller. The low D_0 feature (centered around $(1.9 \pm 0.5) \times 10^{-4}$ μm^2/s) might indicate trapping of EGFRs in plasma membrane compartments, such as

TABLE 1 Comparison of Dynamic Parameters in Different Phases of EGFR Trafficking

Dynamic Parameters	D_{Brn} ($\mu m^2/s$)	L (nm)	D_{micro} ($\mu m^2/s$)	D_{macro} ($\mu m^2/s$)	$\overline{V}_i$ ($\mu m/s$)	V ($\mu m/s$)
Phase I	–	88.0 ± 71.6	(0.9 ± 0.2) × 10^{-3}	(1.7 ± 2.5) × 10^{-3}	0.04 ± 0.02	–
Phase II	(1.3 ± 0.03) × 10^{-3}	96.3 ± 61.8	(1.2 ± 0.2) × 10^{-3}	(5.7 ± 16.2) × 10^{-3}	0.06 ± 0.04	0.24 ± 0.08
Phase III	–	–	–	–	1.20 ± 1.06	1.39 ± 0.99
Phase IV	(1.1 ± 0.02) × 10^{-3}	102.8 ± 65.3	(1.0 ± 0.2) × 10^{-3}	(1.7 ± 3.2) × 10^{-3}	0.05 ± 0.03	–

clathrin-coated pits (89), or formation of EGFR clusters (90). In addition, EGFRs can associate with integrins in a signal transduction system (91). Group 2 trajectories, on the other hand, showed an interchange of Brownian diffusion and confined diffusion, but without any active transport component. Group 3 trajectories exhibited directed diffusion that lasted for at least 0.5 s or longer. Instead of further dividing each trajectory into distinct phases and computing their dynamic parameters separately (as Table 1), here we treated each trajectory as a whole and built histograms of D_0 based on the entire trajectories. The D_0 histograms not only discriminated EGF-stimulated trajectories from no-EGF trajectories, but they also differentiated among EGF-stimulated groups 1, 2, and 3 trajectories themselves (Fig. 5 *B*). Clearly without EGF stimulation, EGFRs were more mobile on the membrane. Dimerization of EGFRs was believed to the cause of reduced mobility for EGF-stimulated EGFRs (50,63), which also induced endocytosis (64). Although untreated EGFRs were more mobile, their time proportions in Brownian and confined diffusion were similar to those of EGF-stimulated EGFRs (Fig. 5 *C*). In addition, no significant differences between trajectories collected from monolayer cells and those from spheroids were noticed.

DISCUSSION

Rationale behind the thresholds used for trajectory classification

How reliably our rolling-average algorithm can identify the motional mode associated with each trajectory segment depends on the thresholds that we select for the classification parameters (scaling exponent α, directional persistence $\Delta\phi$, and confinement index Λ) and the length that we choose for the rolling window (w). Other than the misclassification issue around the change points, 100% classification accuracy cannot be achieved as pure random walks can also transiently exhibit movement similar to confined or directed diffusion (Fig. 2 *B*). Here we use prescribed trajectories embedded with physiologically relevant receptor dynamics (D_{pre}, L_{pre}, and V_{pre}) to train the algorithm and obtain a set of thresholds that minimizes the chance of segment misclassification. For example, movement of an internalized

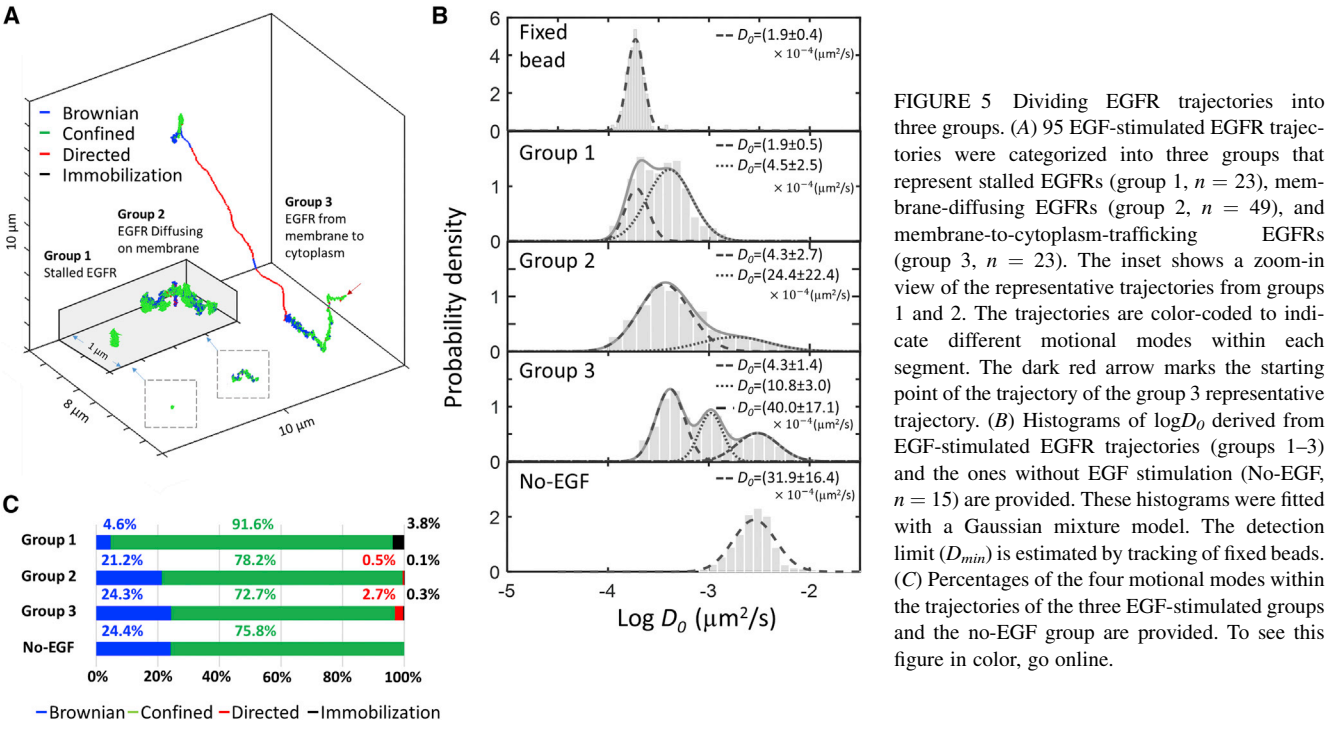

FIGURE 5 Dividing EGFR trajectories into three groups. (*A*) 95 EGF-stimulated EGFR trajectories were categorized into three groups that represent stalled EGFRs (group 1, $n = 23$), membrane-diffusing EGFRs (group 2, $n = 49$), and membrane-to-cytoplasm-trafficking EGFRs (group 3, $n = 23$). The inset shows a zoom-in view of the representative trajectories from groups 1 and 2. The trajectories are color-coded to indicate different motional modes within each segment. The dark red arrow marks the starting point of the trajectory of the group 3 representative trajectory. (*B*) Histograms of logD_0 derived from EGF-stimulated EGFR trajectories (groups 1–3) and the ones without EGF stimulation (No-EGF, $n = 15$) are provided. These histograms were fitted with a Gaussian mixture model. The detection limit (D_{min}) is estimated by tracking of fixed beads. (*C*) Percentages of the four motional modes within the trajectories of the three EGF-stimulated groups and the no-EGF group are provided. To see this figure in color, go online.

early endosome is mostly assisted by molecular motors on microtubules, which exhibits a characteristic transport speed of ~1 μm/s (60,92) with lateral diffusivity ($D_{lateral}$) around 3×10^{-3} $\mu m^2/s$ (53). By analyzing the prescribed trajectories built on these practical dynamic parameters, we confirm that the thresholds of 1.4 for α and 0.1 for $\Delta\phi$ work well in distinguishing active transport from passive transport (Fig. S4). These results also indicate that the length of the rolling window has to be sufficiently long, on the order of 1.6 s, to accurately identify the directed diffusion. Since motor protein-assisted active transport typically lasts for 1–2 s or longer (34,57), the 1.6 s rolling window (w) with 0.1 s sliding time step (Δs) is appropriate to resolve motor protein-assisted directed diffusion.

As for the confinement index Λ, the upper-bound and the lower-bound thresholds for Λ are chosen such that there is a less than 5% probability for Brownian diffusion or immobilization being misidentified as confined diffusion (Fig. S5). Since reliable differentiation of confined diffusion from Brownian diffusion is the most critical classification step in our analysis, we define the "power of confinement detection" to be the successful rate to capture each confined diffusion. We further test these Λ thresholds with different lengths of rolling window and find that the rolling window has to be longer than 1.6 s for the power of confinement detection being greater than 90% (Fig. S5). We emphasize that the thresholds used in our trajectory segmentation and classification method are calibrated computationally (via Monte Carlo simulation, Fig. S5) and validated experimentally (via SME, Figs. 2, S4, and S7). Although here we only demonstrate the analysis of EGFR trajectories, our method should be applicable to many other trajectories acquired from biological samples with minor modifications. The detailed information of threshold optimization and the calculation of these three classification parameters were summarized in Supporting Material (Table S1; Fig. S3).

Challenges in molecular trajectory analysis

Analysis of complex trajectories faces three major challenges: 1) observing transient behaviors in motion patterns that span the spatiotemporal scale from nanometer to micron and from millisecond to second, 2) discriminating mechanisms that give similar subdiffusive MSD curves, and 3) identifying the physical scenarios behind the observed molecular trajectories. In this study we have tackled the first challenge, and future work will focus on the final two. Other than the mechanisms in confined geometries that lead to subdiffusive behaviors (corralled, hop, and cage diffusion, as discussed in Fig. S8), mechanisms in "unconfined" geometries, such as continuous time random walk (93–95), fractional Brownian motion (96,97), and random walk on a fractal structure (98), can also give subdiffusive MSD curves (11,41,99). A sophisticated differentiation decision tree, such as the one proposed by Meroz's group (41), should be established and rigorously tested. Such a decision tree can be used in conjunction with ours in Fig. 1 *B* for identifying the mechanisms behind the subdiffusive behaviors in both confined and unconfined geometries.

Whereas different confinement models and simulations have been carried out by other groups (34,37,39,100) and us (Fig. S8), it is currently difficult to rule out one model (e.g., cage diffusion (69)) from other models (e.g., hop diffusion (100)) when explaining the mechanisms behind the observed confined diffusion. Since MSD fits alone do not fully distinguish between different models for the diffusion, additional information is often needed. For instance, Kusumi's group determined that phospholipids undergo hop diffusion in cell membrane based on the control experiments that modified or depleted membrane skeleton (100). On the other hand, Salome's group believed that a G-protein-coupled receptor follows cage diffusion based on their visual inspection of the trajectories—only few hops from one domain to another were observed (69). With a close examination, our results resemble the hop diffusion described by Kusumi based on 40 nm gold particle tracking (Fig. 3 *A*) (101). Although the conventional 2D-SPT results suggested that all phospholipid and transmembrane proteins exhibit short-term confined diffusion within a compartment and long-term hop movement from one domain to another (so-called the skeleton fence model) (101), more-advanced techniques, such as the scanning STED-FCS that provides even higher spatiotemporal resolution in molecular motion analysis, showed no evidence of nanodomains but rather suggested transient interactions with immobile or slowly moving entities, possibly proteins (102). Since particle size effect on the tracking experiment has not been completely elucidated, hop diffusion as a general molecule diffusion phenomenon on membrane is still under debate (49). Anyhow, it becomes clear that to derive biological meaning from single-particle trajectories, one cannot simply rely on a single analysis tool or a single parameter such as MSD. Proper controls are also critically important.

Trade-offs in temporal resolution and probe size

Although our TSUNAMI microscope is capable of performing 3D tracking at 50 μs temporal resolution (20 kHz) when the tag is very bright (30), in the current experiments the feedback loop was set to be 20 ms so more photons could be collected for a better position estimate. The trade-off of this adjustment is the reduced capacity in resolving transient confinement of EGFRs on plasma membrane. Lagerholm's group has shown that EGFRs are transiently confined in compartments with linear dimension of 100–150 nm and a mean confinement duration of 50–100 ms, using the 2D-SPT method with 1.75kHz frame rate (49). We have observed a similar confinement size in our 3D-SPT experiments (Table 1) but a longer confinement duration. Although high

temporal resolution will certainly improve the estimate of transient confinement duration, significantly larger nanoparticle tag is often needed. Recently Yang's group demonstrated 3D-SPT at 10 μs temporal resolution using a giant polystyrene bead and quantum dot assembly (~100 nm) (79). Although larger (also brighter and more photostable) nanoparticle tags have provided us with excellent localization accuracy and temporal resolution in single-particle tracking, there is generally a doubt that how much these large particles may influence the mobility of molecules under investigation (e.g., by inducing cross-linking with other biomolecules or by blocking molecule's interactions with environment) (11,103). It has been reported that transmembrane proteins tagged with a 40 nm gold nanoparticle could diffuse three to seven times slower than the same proteins tagged with an Alexa 594 dye due to steric hindrance and cross-linking effect (104). EGFRs tagged with a 40 nm gold particle exhibit a diffusivity (~3×10^{-3} $\mu m^2/s$) lower than that of EGFRs tagged with a commercial quantum dot (~0.04 $\mu m^2/s$) (50) or fused with an EGFP (~0.2 $\mu m^2/s$) (106). Although large nanoparticle labels have also been used for high-resolution tracking of a wide range of membrane proteins (such as glycine receptors (107), GPI anchor proteins (17), α-amino-3-hydroxy-5-methyl-4-isoxazolepropionic acid and N-methyl-D-aspartate receptors (108), integrins (109), and cystic fibrosis transmembrane conductance regulator channel proteins (110,111)), smaller particle labels (diameter $<$ 10 nm) are recently developed and tested for SPT in a confined space (such as synaptic receptors in synaptic cleft (27)), providing less steric hindrance and reduced cross-linking. To completely eliminate cross-linking, we are currently developing monovalent EGFR labeling techniques based on site-specific biotinylation of membrane receptors (113), monovalent streptavidin (114,115), and monovalent nanoparticles (116).

Outlook of high-resolution 3D tracking of EGFR

The combination of the TSUNAMI microscope and the classification algorithm is capable of revealing the dynamics of complex EGFR trajectories from the plasma membrane into deep cytoplasm at 20 ms temporal resolution and 16/43 nm (xy/z) spatial resolution, with track duration ranging from 2 to 10 min and vertical tracking depth up to tens of microns. We can monitor the onset of EGFR internalization process (phase II in Fig. 4 *A*) and directly observe the change points of motional modes along the trajectory (Fig. 4 *C*). Since the 2D-SPT techniques can only probe the diffusion process on membrane (phase I) (49,50,58), very few results have been published about the endocytosis and intracellular transport dynamics of membrane receptors (34,60). In this study we report the physical parameters associated with these processes (Table 1) and show the statistics of our 3D trajectory classifications (Fig. 5). Interestingly, our results suggest that there are three populations of EGFRs that respond differently (immobilization, membrane diffusion, and active transportation) upon ligand stimulation. It will be worthwhile to further investigate the molecular mechanisms causing the difference.

Defective endocytosis of EGFR can be caused by altered ubiquitination (117,118), altered cytoskeletal interactions (119), and derailed endocytosis. All of these causes of EGFR dysfunction can be associated with oncogenic alterations (120). Therefore, the outlined 3D-SPT method and trajectory classification would be a highly desirable tool for monitoring EGFR intracellular trafficking dynamics at distinct phenotypic transition stages in cancer development. Additionally, our study may also provide a unique means to identify how the therapeutic drugs (such as monoclonal antibodies and tyrosine kinase inhibitors) affect receptor dynamics (anywhere from actin network reorganization (121) to derailed endocytosis (119)), which could have significant impact in the treatment of cancer.

SUPPORTING MATERIAL

Supporting Materials and Methods, eighteen figures, and one table are available at http://www.biophysj.org/biophysj/supplemental/S0006-3495(16)30875-X.

AUTHOR CONTRIBUTIONS

Y.-L.L. and H.-C.Y. conceived the project and wrote the article. E.P.P. built the microscope and developed the control software. Y.-L.L., E.P.P., and P.Y. performed the 3D tracking experiments. Y.-L.L. and C.L. performed Monte Carlo simulations and developed the trajectory analysis algorithm. Y.-L.L. and P.Y. prepared cell samples and analyzed the data. C.-K.C. and M.-C.H. helped analyze the EGFR trajectories. H.-C.Y. and A.K.D. supervised the project.

ACKNOWLEDGMENTS

We thank Dr. Konstantin V. Sokolov for providing A431 cell line.

This work was supported by Robert A. Welch Foundation (F-1833), Texas 4000, and NIH grants CA193038 and CA109311 (to M.-C.H.).

REFERENCES

1. Shera, E. B., N. K. Seitzinger, …, S. A. Soper. 1990. Detection of single fluorescent molecules. *Chem. Phys. Lett.* 174:553–557.
2. Ambrose, W. P., P. M. Goodwin, …, R. A. Keller. 1999. Single molecule fluorescence spectroscopy at ambient temperature. *Chem. Rev.* 99:2929–2956.
3. Sauer, M., and C. Zander. 2003. Single molecule identification in solution: Principles and applications. *In* Single Molecule Detection in Solution. Wiley-VCH Verlag, Hoboken, NJ, pp. 247–272.
4. Toomre, D., and J. Bewersdorf. 2010. A new wave of cellular imaging. *Annu. Rev. Cell Dev. Biol.* 26:285–314.

5. Betzig, E., G. H. Patterson, …, H. F. Hess. 2006. Imaging intracellular fluorescent proteins at nanometer resolution. *Science.* 313:1642–1645.
6. Hess, S. T., T. P. Girirajan, and M. D. Mason. 2006. Ultra-high resolution imaging by fluorescence photoactivation localization microscopy. *Biophys. J.* 91:4258–4272.
7. Rust, M. J., M. Bates, and X. Zhuang. 2006. Sub-diffraction-limit imaging by stochastic optical reconstruction microscopy (STORM). *Nat. Methods.* 3:793–795.
8. Liu, C., Y.-L. Liu, …, H.-C. Yeh. 2016. Single-molecule tracking and its application in biomolecular binding detection. *IEEE J. Sel. Top. Quantum Electron.* 22:64–76.
9. Axelrod, D., P. Ravdin, …, T. R. Podleski. 1976. Lateral motion of fluorescently labeled acetylcholine receptors in membranes of developing muscle fibers. *Proc. Natl. Acad. Sci. USA.* 73:4594–4598.
10. Magde, D., E. Elson, and W. W. Webb. 1972. Thermodynamic fluctuations in a reacting system—measurement by fluorescence correlation spectroscopy. *Phys. Rev. Lett.* 29:705.
11. Manzo, C., and M. F. Garcia-Parajo. 2015. A review of progress in single particle tracking: from methods to biophysical insights. *Rep. Prog. Phys.* 78:124601.
12. Geerts, H., M. De Brabander, …, P. Hollenbeck. 1987. Nanovid tracking: a new automatic method for the study of mobility in living cells based on colloidal gold and video microscopy. *Biophys. J.* 52:775–782.
13. De Brabander, M., R. Nuydens, …, C. R. Hopkins. 1988. Dynamic behavior of the transferrin receptor followed in living epidermoid carcinoma (A431) cells with nanovid microscopy. *Cell Motil. Cytoskeleton.* 9:30–47.
14. Gelles, J., B. J. Schnapp, and M. P. Sheetz. 1988. Tracking kinesin-driven movements with nanometre-scale precision. *Nature.* 331:450–453.
15. Sheetz, M. P., S. Turney, …, E. L. Elson. 1989. Nanometre-level analysis demonstrates that lipid flow does not drive membrane glycoprotein movements. *Nature.* 340:284–288.
16. Saxton, M. J., and K. Jacobson. 1997. Single-particle tracking: applications to membrane dynamics. *Annu. Rev. Biophys. Biomol. Struct.* 26:373–399.
17. Pinaud, F., X. Michalet, …, S. Weiss. 2009. Dynamic partitioning of a glycosyl-phosphatidylinositol-anchored protein in glycosphingolipid-rich microdomains imaged by single-quantum dot tracking. *Traffic.* 10:691–712.
18. Pinaud, F., S. Clarke, …, M. Dahan. 2010. Probing cellular events, one quantum dot at a time. *Nat. Methods.* 7:275–285.
19. Kusumi, A., T. A. Tsunoyama, …, T. K. Fujiwara. 2014. Tracking single molecules at work in living cells. *Nat. Chem. Biol.* 10:524–532.
20. Yildiz, A., J. N. Forkey, …, P. R. Selvin. 2003. Myosin V walks hand-over-hand: single fluorophore imaging with 1.5-nm localization. *Science.* 300:2061–2065.
21. Toprak, E., H. Balci, …, P. R. Selvin. 2007. Three-dimensional particle tracking via bifocal imaging. *Nano Lett.* 7:2043–2045.
22. Ram, S., P. Prabhat, …, R. J. Ober. 2008. High accuracy 3D quantum dot tracking with multifocal plane microscopy for the study of fast intracellular dynamics in live cells. *Biophys. J.* 95:6025–6043.
23. McHale, K., A. J. Berglund, and H. Mabuchi. 2007. Quantum dot photon statistics measured by three-dimensional particle tracking. *Nano Lett.* 7:3535–3539.
24. Katayama, Y., O. Burkacky, …, D. C. Lamb. 2009. Real-time nanomicroscopy via three-dimensional single-particle tracking. *ChemPhysChem.* 10:2458–2464.
25. Levi, V., Q. Ruan, and E. Gratton. 2005. 3-D particle tracking in a two-photon microscope: application to the study of molecular dynamics in cells. *Biophys. J.* 88:2919–2928.
26. Pavani, S. R. P., M. A. Thompson, …, W. E. Moerner. 2009. Three-dimensional, single-molecule fluorescence imaging beyond the diffraction limit by using a double-helix point spread function. *Proc. Natl. Acad. Sci. USA.* 106:2995–2999.
27. Cai, E., P. Ge, …, P. R. Selvin. 2014. Stable small quantum dots for synaptic receptor tracking on live neurons. *Angew. Chem. Int. Ed. Engl.* 53:12484–12488.
28. Cang, H., C. M. Wong, …, H. Yang. 2006. Confocal three dimensional tracking of a single nanoparticle with concurrent spectroscopic readouts. *Appl. Phys. Lett.* 88:223901.
29. Wells, N. P., G. A. Lessard, and J. H. Werner. 2008. Confocal, three-dimensional tracking of individual quantum dots in high-background environments. *Anal. Chem.* 80:9830–9834.
30. Perillo, E., Y.-L. Liu, …, A. K. Dunn. 2015. Deep and high-resolution three-dimensional tracking of single particles using nonlinear and multiplexed illumination. *Nat. Commun.* 6:7874.
31. Perillo, E., Y.-L. Liu, …, A. K. Dunn. 2015. Single particle tracking through highly scattering media with multiplexed two-photon excitation. *SPIE Proc.* 9331:933107.
32. Liu, C., E. P. Perillo, …, H.-C. Yeh. 2014. 3D single-molecule tracking using one- and two-photon excitation microscopy. *SPIE Proc.* 8950:89501C.
33. Liu, C., Y.-L. Liu, …, H.-C. Yeh. 2015. Improving z-tracking accuracy in the two-photon single-particle tracking microscope. *Appl. Phys. Lett.* 107:153701.
34. Huet, S., E. Karatekin, …, J. P. Henry. 2006. Analysis of transient behavior in complex trajectories: application to secretory vesicle dynamics. *Biophys. J.* 91:3542–3559.
35. Kusumi, A., Y. Sako, and M. Yamamoto. 1993. Confined lateral diffusion of membrane receptors as studied by single particle tracking (nanovid microscopy). Effects of calcium-induced differentiation in cultured epithelial cells. *Biophys. J.* 65:2021–2040.
36. Arcizet, D., B. Meier, …, D. Heinrich. 2008. Temporal analysis of active and passive transport in living cells. *Phys. Rev. Lett.* 101:248103.
37. Meilhac, N., L. Le Guyader, …, N. Destainville. 2006. Detection of confinement and jumps in single-molecule membrane trajectories. *Phys. Rev. E Stat. Nonlin. Soft Matter Phys.* 73:011915.
38. Montiel, D., H. Cang, and H. Yang. 2006. Quantitative characterization of changes in dynamical behavior for single-particle tracking studies. *J. Phys. Chem. B.* 110:19763–19770.
39. Di Rienzo, C., E. Gratton, …, F. Cardarelli. 2013. Fast spatiotemporal correlation spectroscopy to determine protein lateral diffusion laws in live cell membranes. *Proc. Natl. Acad. Sci. USA.* 110:12307–12312.
40. Tabei, S. M. A., S. Burov, …, N. F. Scherer. 2013. Intracellular transport of insulin granules is a subordinated random walk. *Proc. Natl. Acad. Sci. USA.* 110:4911–4916.
41. Meroz, Y., and I. M. Sokolov. 2015. A toolbox for determining subdiffusive mechanisms. *Phys. Rep.* 573:1–29.
42. Chen, K., B. Wang, …, S. Granick. 2013. Diagnosing heterogeneous dynamics in single-molecule/particle trajectories with multiscale wavelets. *ACS Nano.* 7:8634–8644.
43. Simson, R., E. D. Sheets, and K. Jacobson. 1995. Detection of temporary lateral confinement of membrane proteins using single-particle tracking analysis. *Biophys. J.* 69:989–993.
44. Helmuth, J. A., C. J. Burckhardt, …, I. F. Sbalzarini. 2007. A novel supervised trajectory segmentation algorithm identifies distinct types of human adenovirus motion in host cells. *J. Struct. Biol.* 159:347–358.
45. Feder, T. J., I. Brust-Mascher, …, W. W. Webb. 1996. Constrained diffusion or immobile fraction on cell surfaces: a new interpretation. *Biophys. J.* 70:2767–2773.
46. Saxton, M. J. 1994. Anomalous diffusion due to obstacles: a Monte Carlo study. *Biophys. J.* 66:394–401.
47. Persson, F., M. Lindén, …, J. Elf. 2013. Extracting intracellular diffusive states and transition rates from single-molecule tracking data. *Nat. Methods.* 10:265–269.

48. Bosch, P. J., J. S. Kanger, and V. Subramaniam. 2014. Classification of dynamical diffusion states in single molecule tracking microscopy. *Biophys. J.* 107:588–598.

49. Clausen, M. P., and B. C. Lagerholm. 2013. Visualization of plasma membrane compartmentalization by high-speed quantum dot tracking. *Nano Lett.* 13:2332–2337.

50. Low-Nam, S. T., K. A. Lidke, …, D. S. Lidke. 2011. ErbB1 dimerization is promoted by domain co-confinement and stabilized by ligand binding. *Nat. Struct. Mol. Biol.* 18:1244–1249.

51. Das, R., C. W. Cairo, and D. Coombs. 2009. A hidden Markov model for single particle tracks quantifies dynamic interactions between LFA-1 and the actin cytoskeleton. *PLOS Comput. Biol.* 5:e1000556.

52. Ott, D., P. M. Bendix, and L. B. Oddershede. 2013. Revealing hidden dynamics within living soft matter. *ACS Nano.* 7:8333–8339.

53. Fakhri, N., A. D. Wessel, …, C. F. Schmidt. 2014. High-resolution mapping of intracellular fluctuations using carbon nanotubes. *Science.* 344:1031–1035.

54. Ahmed, W. W., B. J. Williams, …, T. A. Saif. 2013. Measuring nonequilibrium vesicle dynamics in neurons under tension. *Lab Chip.* 13:570–578.

55. Ahmed, W. W., and T. A. Saif. 2014. Active transport of vesicles in neurons is modulated by mechanical tension. *Sci. Rep.* 4:4481.

56. Türkcan, S., and J. B. Masson. 2013. Bayesian decision tree for the classification of the mode of motion in single-molecule trajectories. *PLoS One.* 8:e82799.

57. Chen, K., B. Wang, and S. Granick. 2015. Memoryless self-reinforcing directionality in endosomal active transport within living cells. *Nat. Mater.* 14:589–593.

58. Sergé, A., N. Bertaux, …, D. Marguet. 2008. Dynamic multiple-target tracing to probe spatiotemporal cartography of cell membranes. *Nat. Methods.* 5:687–694.

59. Trinczek, B., A. Ebneth, …, E. Mandelkow. 1999. Tau regulates the attachment/detachment but not the speed of motors in microtubule-dependent transport of single vesicles and organelles. *J. Cell Sci.* 112:2355–2367.

60. de Bruin, K., N. Ruthardt, …, C. Bräuchle. 2007. Cellular dynamics of EGF receptor-targeted synthetic viruses. *Mol. Ther.* 15:1297–1305.

61. Nielsen, E., F. Severin, …, M. Zerial. 1999. Rab5 regulates motility of early endosomes on microtubules. *Nat. Cell Biol.* 1:376–382.

62. Ichikawa, T., M. Yamada, …, S. Kawato. 2000. Digital fluorescence imaging of trafficking of endosomes containing low-density lipoprotein in brain astroglial cells. *Biochem. Biophys. Res. Commun.* 269:25–30.

63. Chung, I., R. Akita, …, I. Mellman. 2010. Spatial control of EGF receptor activation by reversible dimerization on living cells. *Nature.* 464:783–787.

64. Johannessen, L. E., N. M. Pedersen, …, E. Stang. 2006. Activation of the epidermal growth factor (EGF) receptor induces formation of EGF receptor- and Grb2-containing clathrin-coated pits. *Mol. Cell. Biol.* 26:389–401.

65. Izeddin, I., V. Récamier, …, X. Darzacq. 2014. Single-molecule tracking in live cells reveals distinct target-search strategies of transcription factors in the nucleus. *eLife.* 3:e02230.

66. Knight, S. C., L. Xie, …, R. Tjian. 2015. Dynamics of CRISPR-Cas9 genome interrogation in living cells. *Science.* 350:823–826.

67. Höfling, F., and T. Franosch. 2013. Anomalous transport in the crowded world of biological cells. *Rep. Prog. Phys.* 76:046602.

68. Qian, H., M. P. Sheetz, and E. L. Elson. 1991. Single particle tracking. Analysis of diffusion and flow in two-dimensional systems. *Biophys. J.* 60:910–921.

69. Daumas, F., N. Destainville, …, L. Salomé. 2003. Confined diffusion without fences of a g-protein-coupled receptor as revealed by single particle tracking. *Biophys. J.* 84:356–366.

70. Vestergaard, C. L., P. C. Blainey, and H. Flyvbjerg. 2014. Optimal estimation of diffusion coefficients from single-particle trajectories. *Phys. Rev. E Stat. Nonlin. Soft Matter Phys.* 89:022726.

71. Johns, L. M., E. S. Levitan, …, D. Axelrod. 2001. Restriction of secretory granule motion near the plasma membrane of chromaffin cells. *J. Cell Biol.* 153:177–190.

72. Ng, Y.-K., X. Lu, …, E. S. Levitan. 2003. Unexpected mobility variation among individual secretory vesicles produces an apparent refractory neuropeptide pool. *Biophys. J.* 84:4127–4134.

73. Clausen, M. P., E. C. Arnspang, …, B. C. Lagerholm. 2014. Simultaneous multi-species tracking in live cells with quantum dot conjugates. *PLoS One.* 9:e97671.

74. Lang, T., I. Wacker, …, W. Almers. 2000. Role of actin cortex in the subplasmalemmal transport of secretory granules in PC-12 cells. *Biophys. J.* 78:2863–2877.

75. Manneville, J.-B., S. Etienne-Manneville, …, M. Ferenczi. 2003. Interaction of the actin cytoskeleton with microtubules regulates secretory organelle movement near the plasma membrane in human endothelial cells. *J. Cell Sci.* 116:3927–3938.

76. Friedrich, J., C. Seidel, …, L. A. Kunz-Schughart. 2009. Spheroid-based drug screen: considerations and practical approach. *Nat. Protoc.* 4:309–324.

77. Pons, T., H. T. Uyeda, …, H. Mattoussi. 2006. Hydrodynamic dimensions, electrophoretic mobility, and stability of hydrophilic quantum dots. *J. Phys. Chem. B.* 110:20308–20316.

78. Sigismund, S., E. Argenzio, …, P. P. Di Fiore. 2008. Clathrin-mediated internalization is essential for sustained EGFR signaling but dispensable for degradation. *Dev. Cell.* 15:209–219.

79. Welsher, K., and H. Yang. 2014. Multi-resolution 3D visualization of the early stages of cellular uptake of peptide-coated nanoparticles. *Nat. Nanotechnol.* 9:198–203.

80. Wells, N. P., G. A. Lessard, …, J. H. Werner. 2010. Time-resolved three-dimensional molecular tracking in live cells. *Nano Lett.* 10:4732–4737.

81. Jaqaman, K., H. Kuwata, …, S. Grinstein. 2011. Cytoskeletal control of CD36 diffusion promotes its receptor and signaling function. *Cell.* 146:593–606.

82. Kaksonen, M., C. P. Toret, and D. G. Drubin. 2006. Harnessing actin dynamics for clathrin-mediated endocytosis. *Nat. Rev. Mol. Cell Biol.* 7:404–414.

83. Kaksonen, M., C. P. Toret, and D. G. Drubin. 2005. A modular design for the clathrin- and actin-mediated endocytosis machinery. *Cell.* 123:305–320.

84. Merrifield, C. J., M. E. Feldman, …, W. Almers. 2002. Imaging actin and dynamin recruitment during invagination of single clathrin-coated pits. *Nat. Cell Biol.* 4:691–698.

85. Kural, C., H. Kim, …, P. R. Selvin. 2005. Kinesin and dynein move a peroxisome in vivo: a tug-of-war or coordinated movement? *Science.* 308:1469–1472.

86. Soppina, V., A. K. Rai, …, R. Mallik. 2009. Tug-of-war between dissimilar teams of microtubule motors regulates transport and fission of endosomes. *Proc. Natl. Acad. Sci. USA.* 106:19381–19386.

87. Hendricks, A. G., E. Perlson, …, E. L. Holzbaur. 2010. Motor coordination via a tug-of-war mechanism drives bidirectional vesicle transport. *Curr. Biol.* 20:697–702.

88. Gross, S. P., M. A. Welte, …, E. F. Wieschaus. 2000. Dynein-mediated cargo transport in vivo. A switch controls travel distance. *J. Cell Biol.* 148:945–956.

89. Li, Y., L. Shang, and G. U. Nienhaus. 2016. Super-resolution imaging-based single particle tracking reveals dynamics of nanoparticle internalization by live cells. *Nanoscale.* 8:7423–7429.

90. Kotani, N., J. Gu, …, K. Honke. 2008. Biochemical visualization of cell surface molecular clustering in living cells. *Proc. Natl. Acad. Sci. USA.* 105:7405–7409.

91. Moro, L., L. Dolce, …, P. Defilippi. 2002. Integrin-induced epidermal growth factor (EGF) receptor activation requires c-Src and p130Cas

and leads to phosphorylation of specific EGF receptor tyrosines. *J. Biol. Chem.* 277:9405–9414.

92. Ruthardt, N., D. C. Lamb, and C. Bräuchle. 2011. Single-particle tracking as a quantitative microscopy-based approach to unravel cell entry mechanisms of viruses and pharmaceutical nanoparticles. *Mol. Ther.* 19:1199–1211.
93. Weigel, A. V., B. Simon, …, D. Krapf. 2011. Ergodic and nonergodic processes coexist in the plasma membrane as observed by single-molecule tracking. *Proc. Natl. Acad. Sci. USA.* 108:6438–6443.
94. Jeon, J.-H., V. Tejedor, …, R. Metzler. 2011. In vivo anomalous diffusion and weak ergodicity breaking of lipid granules. *Phys. Rev. Lett.* 106:048103.
95. Metzler, R., and J. Klafter. 2000. The random walk's guide to anomalous diffusion: a fractional dynamics approach. *Phys. Rep.* 339:1–77.
96. Burnecki, K., E. Kepten, …, A. Weron. 2012. Universal algorithm for identification of fractional Brownian motion. A case of telomere subdiffusion. *Biophys. J.* 103:1839–1847.
97. Ernst, D., M. Hellmann, …, M. Weiss. 2012. Fractional Brownian motion in crowded fluids. *Soft Matter.* 8:4886–4889.
98. Meroz, Y., I. M. Sokolov, and J. Klafter. 2010. Subdiffusion of mixed origins: when ergodicity and nonergodicity coexist. *Phys. Rev. E Stat. Nonlin. Soft Matter Phys.* 81:010101.
99. Metzler, R., J. H. Jeon, …, E. Barkai. 2014. Anomalous diffusion models and their properties: non-stationarity, non-ergodicity, and ageing at the centenary of single particle tracking. *Phys. Chem. Chem. Phys.* 16:24128–24164.
100. Fujiwara, T., K. Ritchie, …, A. Kusumi. 2002. Phospholipids undergo hop diffusion in compartmentalized cell membrane. *J. Cell Biol.* 157:1071–1081.
101. Kusumi, A., Y. M. Shirai, …, T. K. Fujiwara. 2010. Hierarchical organization of the plasma membrane: investigations by single-molecule tracking vs. fluorescence correlation spectroscopy. *FEBS Lett.* 584:1814–1823.
102. Honigmann, A., V. Mueller, …, C. Eggeling. 2014. Scanning STED-FCS reveals spatiotemporal heterogeneity of lipid interaction in the plasma membrane of living cells. *Nat. Commun.* 5:5412.
103. Clausen, M. P., and B. C. Lagerholm. 2011. The probe rules in single particle tracking. *Curr. Protein Pept. Sci.* 12:699–713.
104. Umemura, Y. M., M. Vrljic, …, A. Kusumi. 2008. Both MHC class II and its GPI-anchored form undergo hop diffusion as observed by single-molecule tracking. *Biophys. J.* 95:435–450.
106. Bag, N., S. Huang, and T. Wohland. 2015. Plasma membrane organization of epidermal growth factor receptor in resting and ligand-bound states. *Biophys. J.* 109:1925–1936.
107. Dahan, M., S. Lévi, …, A. Triller. 2003. Diffusion dynamics of glycine receptors revealed by single-quantum dot tracking. *Science.* 302:442–445.
108. Groc, L., M. Heine, …, D. Choquet. 2004. Differential activity-dependent regulation of the lateral mobilities of AMPA and NMDA receptors. *Nat. Neurosci.* 7:695–696.
109. Chen, H., I. Titushkin, …, M. Cho. 2007. Altered membrane dynamics of quantum dot-conjugated integrins during osteogenic differentiation of human bone marrow derived progenitor cells. *Biophys. J.* 92:1399–1408.
110. Bates, I. R., B. Hébert, …, J. W. Hanrahan. 2006. Membrane lateral diffusion and capture of CFTR within transient confinement zones. *Biophys. J.* 91:1046–1058.
111. Haggie, P. M., J. K. Kim, …, A. S. Verkman. 2006. Tracking of quantum dot-labeled CFTR shows near immobilization by C-terminal PDZ interactions. *Mol. Biol. Cell.* 17:4937–4945.
113. Liu, A. P., F. Aguet, …, S. L. Schmid. 2010. Local clustering of transferrin receptors promotes clathrin-coated pit initiation. *J. Cell Biol.* 191:1381–1393.
114. Howarth, M., D. J. Chinnapen, …, A. Y. Ting. 2006. A monovalent streptavidin with a single femtomolar biotin binding site. *Nat. Methods.* 3:267–273.
115. Chamma, I., M. Letellier, …, O. Thoumine. 2016. Mapping the dynamics and nanoscale organization of synaptic adhesion proteins using monomeric streptavidin. *Nat. Commun.* 7:10773.
116. Farlow, J., D. Seo, …, Y. W. Jun. 2013. Formation of targeted monovalent quantum dots by steric exclusion. *Nat. Methods.* 10:1203–1205.
117. Yarden, Y. 2001. The EGFR family and its ligands in human cancer. Signalling mechanisms and therapeutic opportunities. *Eur. J. Cancer.* 37 (*Suppl. 4*):S3–S8.
118. Gan, Y., C. Shi, …, Y. Huang. 2010. Differential roles of ERK and Akt pathways in regulation of EGFR-mediated signaling and motility in prostate cancer cells. *Oncogene.* 29:4947–4958.
119. Mosesson, Y., G. B. Mills, and Y. Yarden. 2008. Derailed endocytosis: an emerging feature of cancer. *Nat. Rev. Cancer.* 8:835–850.
120. Casaletto, J. B., and A. I. McClatchey. 2012. Spatial regulation of receptor tyrosine kinases in development and cancer. *Nat. Rev. Cancer.* 12:387–400.
121. Vega, F. M., and A. J. Ridley. 2008. Rho GTPases in cancer cell biology. *FEBS Lett.* 582:2093–2101.

Biophysical Journal, Volume *111*

Supplemental Information

Segmentation of 3D Trajectories Acquired by TSUNAMI Microscope: An Application to EGFR Trafficking

Yen-Liang Liu, Evan P. Perillo, Cong Liu, Peter Yu, Chao-Kai Chou, Mien-Chie Hung, Andrew K. Dunn, and Hsin-Chih Yeh

Supplementary Information

Segmentation of 3D Trajectories Acquired by TSUNAMI Microscope:
An Application to EGFR Trafficking

Yen-Liang Liu[1], Evan P. Perillo[1], Cong Liu[1], Peter Yu[1], Chao-Kai Chou[2, 3], Mien-Chie Hung[2,3], Andrew K. Dunn[1] & Hsin-Chih Yeh[1]*

[1]Department of Biomedical Engineering, University of Texas at Austin, Austin, TX, USA; [2]Department of Molecular and Cellular Oncology, The University of Texas MD Anderson Cancer Center, Houston, TX, USA; [3]Center for Molecular Medicine and Graduate Institute of Cancer Biology, China Medical University, Taichung, Taiwan.

Content

Monte Carlo simulations of EGFR movement in live cells

We performed five different sets of Monte Carlo simulations to generate 3D trajectories *in silico* that mimicked (*i*) Brownian diffusion; (*ii*) corralled diffusion in confinements with impermeable boundaries; (*iii*) hop diffusion in confinements with permeable boundaries; (*iv*) cage diffusion in vesicles that themselves can diffuse; and (*v*) directed motion along linear tracks with lateral diffusivity. Brownian diffusion simulations were performed by generating a set of random displacements ($\Delta x, \Delta y, \Delta z$) at each time step. These displacements followed a normal distribution with the following standard deviation:

$$\sigma_{x,y,z} = (2D_{Brn}\,\Delta t)^{1/2}$$

where D_{Brn} is the given diffusion coefficient and Δt is the time step used in simulation. In our simulation, D_{Brn} ranged from 0.01 to 0.16 μm/s^2, which were close to the reported EGFR diffusivities (tagged with a nanoparticle and diffusing on the plasma membrane) (1-3). Corralled diffusion simulations were performed by having a particle freely diffuse in cubes (D_{micro}) with impermeable boundaries and linear sizes (L) of 25, 50, 100 and 200 nm. If particles attempt to penetrate the boundaries of any dimension, the random displacement in the specific dimension(s) will be zero at this time step. Hop diffusion simulations were performed by having a particle freely diffuse in cubes (D_{micro}) with the same linear sizes, but now cubes had permeable boundaries (probability of penetration per attempt P = 0.01). The selected cube sizes were close to the 40 to 300 nm linear compartment sizes reported by other groups (2, 4, 5). Cage diffusion simulations were performed by having a particle freely diffuse within vesicles with impermeable boundaries and diameters (⌀) of 25, 50, 100 and 200 nm. Vesicles themselves were also diffusing ($D_{vesicle}$). These simulations were performed with D_{micro} = 0.5 μm^2/s and $D_{vesicle}$ = 0.01 μm^2/s. Corralled, hop and cage diffusion are all considered as "confined diffusion". Directed diffusion simulations were performed along linear tracks with active transport speeds (V) and lateral diffusivities ($D_{lateral}$). The movement of an internalized early endosome is mostly assisted by molecular motors on microtubules, therefore showing a characteristic transport speed (V) about 1 μm/s (6, 7) with lateral diffusivity ($D_{lateral}$) around 0.003 μm^2/s (8). The directed diffusion simulations were performed with V = 0.5 and 1 μm/s, and $D_{lateral}$ = 0.0025, 0.005, 0.01 and 0.02 μm^2/s. All simulations were performed with the time step (Δt) of 2.5 ms.

Simulation and experiment statements

For **Figures S5** and **S8**, the Monte Carlo simulations were performed for 10 s per run and 100 runs per case. White Gaussian noise type of tracking error (μ_{error} = 0 and σ_{error} = 15 nm) was added to the Monte Carlo simulation generated trajectories before being analyzed by the developed algorithm. The rolling window of 1.6 s (w) and the sliding time step of 0.1 s (Δs) were used to analyze the stimulated trajectories (time step Δt = 2.5 ms).

For **Figures S4**, **S9, S10-13**, the simulated movement experiments (SME) were performed for 30 s per run and 10 runs per case. ⌀200 nm fluorescent beads (F-8810, Thermo Fisher Scientific) were embedded in 1.3% agarose within chambered coverglass at 20 pM. Monte-Carlo-simulation-generated trajectories (without the white noise error) were used to command the movement of the xyz piezo stage every 2.5 ms. Although there were finite differences between the Monte-Carlo-simulation-generated trajectory and the actual trajectory that the stage performed (output from the capacitance sensors in the xyz piezo stage), we conveniently called both these two trajectories the prescribed trajectories. The xyz piezo stage moved once every 2.5 ms and the capacitance sensor recorded the piezo stage voltages every 1 ms, while the integration period of TSUNAMI

microscope was 5 ms. The rolling window of 1.6 s (w) and the sliding time step of 0.1 s (Δs) were used to analyze the experimental trajectories (time step Δt = 5 ms).

Data processing

All data processing was performed in MATLAB (Mathworks). Saved in a binary format, the trajectory raw data contained photon counts and voltage outputs from the actuators (i.e. the xy scanning galvo mirrors (6125H, Cambridge Technology) and the objective z-piezo stage (P-726 PIFOC, PI)) at each time point. Conversion of voltage outputs to particle xyz positions was carried out by multiplying a gain factor for each axis. Trajectories were plotted by simply connecting particle positions of consecutive time points. The particle-trajectory-derived diffusivities of membrane proteins were previously shown to have a broad distribution (9, 10) due to membrane heterogeneity (9). Rather than normal distribution, lognormal distribution was often used to describe the broad distribution of particle-trajectory-derived diffusivity (9, 10). We also observed this trend of lognormal distribution for our particle-trajectory-derived D_{Brn}, D_{micro}, D_{macro}, D_0, V, V_i and L values. The histograms of log$D$, log$V$ and log$L$ were fitted with a Gaussian mixture model (MATLAB, MathWorks). The fitted arithmetic means (μ) and standard deviations (σ) of log$D$, Log$V$, *and* log$L$ were converted to arithmetic means and standard deviations in a linear scale (11).

Optimization of thresholds used for classification

The calculations of these three classification parameters, the scaling component (α) of MSD curves, the directional persistence ($\Delta\phi$), and the confinement index (Λ) were shown in **Figure S3**. The schematic in **Figure S3** also demonstrate the difference of classification parameters in various motional modes.

Table S1 summarized the threshold optimization for the segmentation and classification algorithm. To find out the optimal rolling window length for our segmentation analysis, we calculated scaling exponents α and directional persistence $\Delta\phi$ of directed diffusion SME trajectories (**Figure S4**). The scaling exponent and directional persistence are functions of width of rolling window (w), lateral diffusion coefficient (D_{Lat}), and speed of active transport (V). To set the thresholds to differentiate directed diffusion from passive motion, SME with a set of various w, D_{Lat} , and V were tested and evaluated to determine the optimal w and the thresholds of α and $\Delta\phi$ (**Figure S4**). The simulation parameters (D_{Lat} and V) were referred to values observed in live cells. The D_{Lat} of an endosome conducting active transport in live cell is usually less than 0.01 $\mu m^2/s$ (12, 13), and the V ranges from 0.3 to 2 μm/s (8, 13, 14).

The confinement levels were calibrated with Monte Carlo simulations of Brownian diffusion, confined diffusion, and immobilization (**Figure S5**). The Λ_{Brn} would be a constant under the assumption that D_{max} equals to D_{Brn} (15). To analyze tracking trajectories, the D_{max} need to be derived from experimental trajectories. The Λ_{Im} is determined by the detection limit of tracking system (tracking error (σ_{error}), **Figure S6**) (16). The confinement levels of these three motional modes were defined by Λ_{Brn} and Λ_{Im}. The test of differentiating confined diffusion from Brownian diffusion were conduct in SME (**Figure S7**).

Flow chart for threshold optimiaztion

- Thresholding of α, $\Delta\phi$, and w

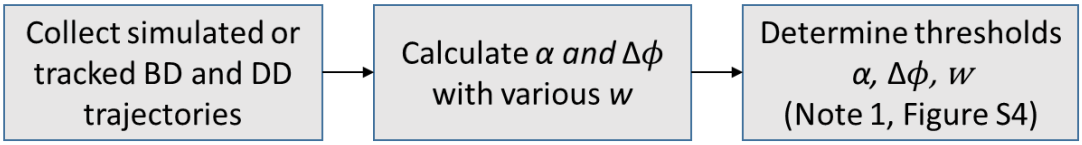

- Thresholding of Λ_{Brn}, Λ_{con}, and Λ_{Im}

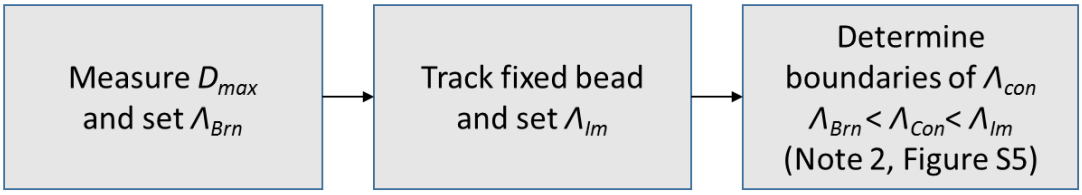

Table S1 | Threshold optimization

Classification parameters	Calibration models (Monte Carlo Simulation)	Threshold values	Note
$\alpha = f_1(w, D_{Lat}, V)$ $\Delta\phi = f_2(w, D_{Lat}, V)$	**Directed diffusion (DD)** D_{Lat} = 0.0025-0.02 μm^2/s V = 0.5, 1 μm/s w = 0.06-1.6 s σ_{error}= 15 nm	• Directed diffuison $\begin{cases}\alpha > 1.4\\ \Delta\phi < 0.1\end{cases}$ • Passive motion $\begin{cases}\alpha < 1.4\\ \Delta\phi > 0.1\end{cases}$ • w = 1.6 s	**1.1** The thresholds of w, α, and $\Delta\phi$ were determined by the SME results (Figure S4). **1.2** If the D_{Lat} of directed diffusion is greater than 0.02 μm^2/s or V is slower than 0.5 μm/s, the w might need to be increased to identify directed diffusion.
$\Lambda = f_3(w, D, D_{max}, L)$	**Brownian diffusion (BD)** D = 0.08 μm^2/s **Confined diffusion (CD)** D = 0.08 μm^2/s L = 25-1000 nm **Immobilization (IM)** σ_{error}= 15 nm	• BD: $\Lambda \leq \Lambda_{Brn}$ • CD: $\Lambda_{Brn} < \Lambda < \Lambda_{Im}$ • IM: $\Lambda \geq \Lambda_{Im}$ • Λ_{Brn} = 14.32 • Λ_{Im} = 677.59 • w = 1.6 s	**2.1** D_{max} is the cutoff of top 5% of diffusion coefficients derived from all trajectories, and D_{max} is assumed to be the D_{Brn} in live cells. The Λ of Brownian diffusion would be independent of w. **2.2** The Λ_{Brn} is defined as the cutoff of top 5% of Λ derived from Brownian diffusion. The Λ_{Brn} will be a constant if D_{max} equals to D_{Brn}. **2.3** The Λ_{Im} is determined by tracking error and defined as the cutoff of bottom 5% of Λ derived from immobilization trajectories.

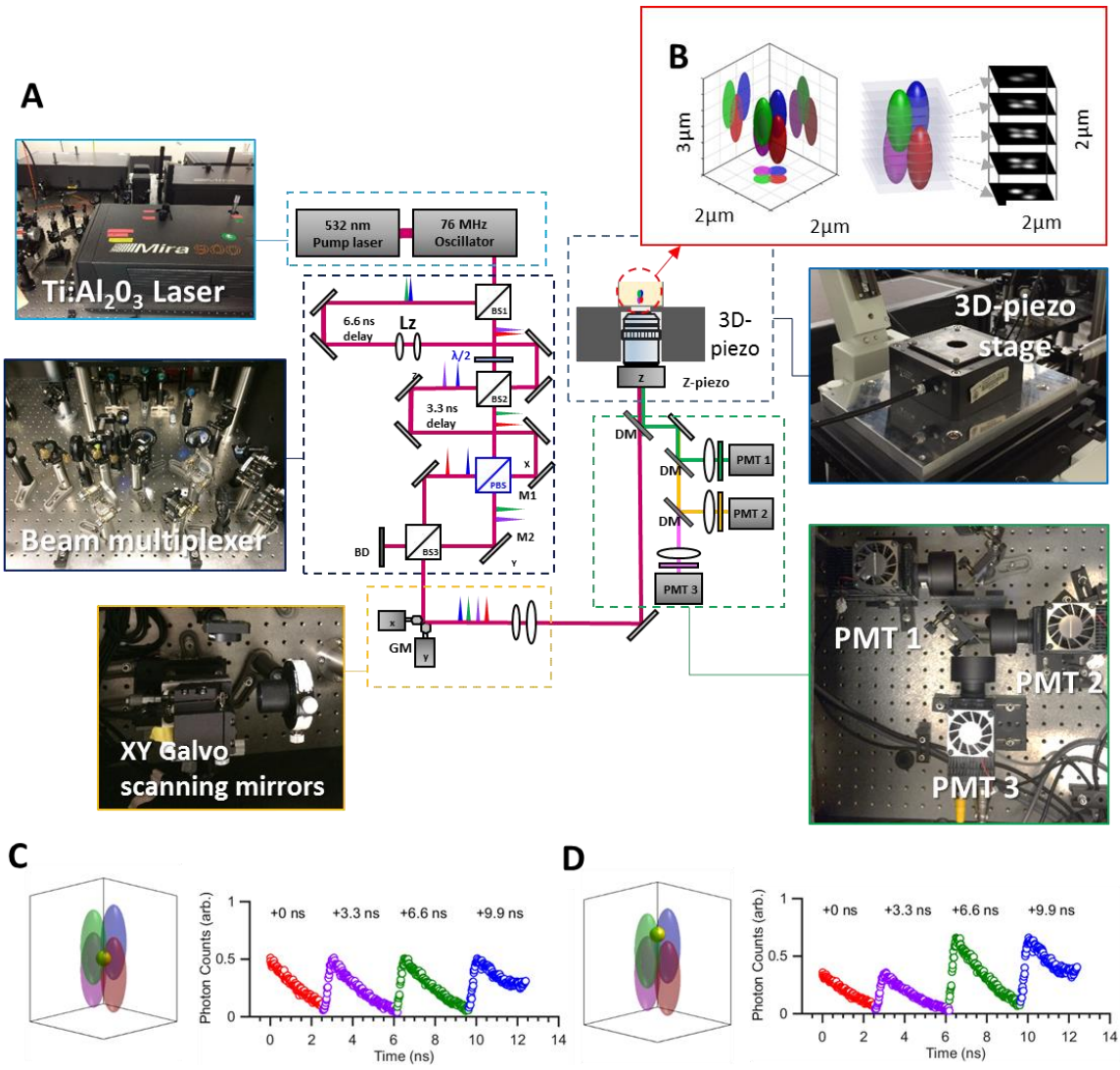

Figure S1 | TSUNAMI microscope setup (including the independent xyz piezo stage for SME) **(A)** The schematic and photograph of the Schematics of TSUNAMI (Tracking of Single particles Using Nonlinear And Multiplexed Illumination) 3D tracking microscope (17). The pulsed laser (76 MHz from a Ti-sapphire laser) is separated into four beams, which are delayed by 3.3 ns each and focused through a high-N.A. objective, generating four barely overlapped two-photon excitation volumes (colored oval balls in **(B)).** Using time-correlated-single-photon counting (TCSPC) detection, each detected photon attributed from an individual excitation volume is assigned to a specific time gated fluorescence decay histogram. An offset of the particle from the tetrahedron center can be estimated from the normalized photon count differences in the four time gates. As described in the paper, an independent xyz piezo stage (P-733K130, PI) is added to the system for SME, which allows us to quantify the tracking error of TSUNAMI microscope. *Lz*: lens set for z-offset control; *BS*: beam splitter; *λ/2*: half-wave plate; *PBS*: polarizing beam splitter; *DM*: dichroic mirror; *BD*: beam dump; *GM*: galvo mirrors; *M*: steering mirrors; *PMT*: photomultiplier tube. **(C)** When the particle (the golden sphere) sits right at the center of the illumination tetrahedron, photon counts are about equal in the four histograms. **(D)** The photon counts in the four histograms fluctuate according to the position of particle in the illumination tetrahedron.

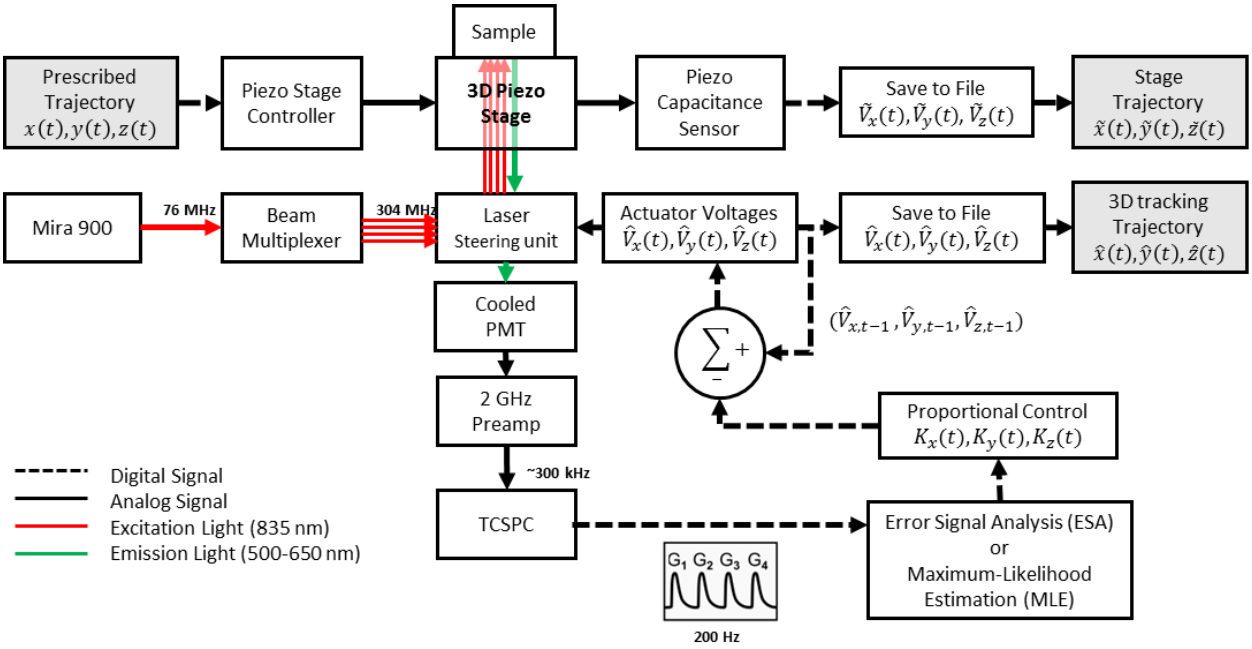

Figure S2 | TSUNAMI feed-back control schematic (including scheme for SME)

A Control Schematic demonstrating system level interaction, feedback control loop, and prescribed motion driven by an xyz piezo stage. The 835 nm excitation ray generated by a Ti:Al_2O_3 laser (Mira 900, Coherent) at 76 MHz repetition rate passes through the beam multiplexer and creates an illumination tetrahedron onto the sample. The sample is driven by an independent xyz piezo stage with a prescribed trajectory ($x(t), y(t), z(t)$). The piezo controller can simultaneously generate defined motion and record the corresponding motion profile which is then converted to a stage trajectory ($\tilde{x}(t), \tilde{y}(t), \tilde{z}(t)$). Fluorescence is detected by a cooled low dark count PMT (H7422PA-40, Hamamatsu Corp.) and amplified with a 2 GHz cutoff bandwidth preamplifier (HFAC-26, Becker and Hickl GmbH). The amplified signal is then measured and correlated to the reference clock of the Ti:Al_2O_3 laser with a TCSPC board (SPC-150, Becker and Hickl GmbH). Every 1-20 ms a photon histogram is sampled from the TCSPC module and processed in the software loop run in LabVIEW (National Instruments). The tracking algorithm employs a proportional control to convert the error signals to new stage positions. Furthermore, Liu and coworkers have demonstrated that the z-tracking accuracy can be significantly increased using maximum likelihood estimations (MLE) (18). New voltages are sent out through a DAQ (PCIe-6353, National Instruments) to their respective actuators, galvo mirrors for X and Y, piezo objective stage for Z. The saved voltages are converted to a 3D tracking trajectory ($\hat{x}(t), \hat{y}(t), \hat{z}(t)$).

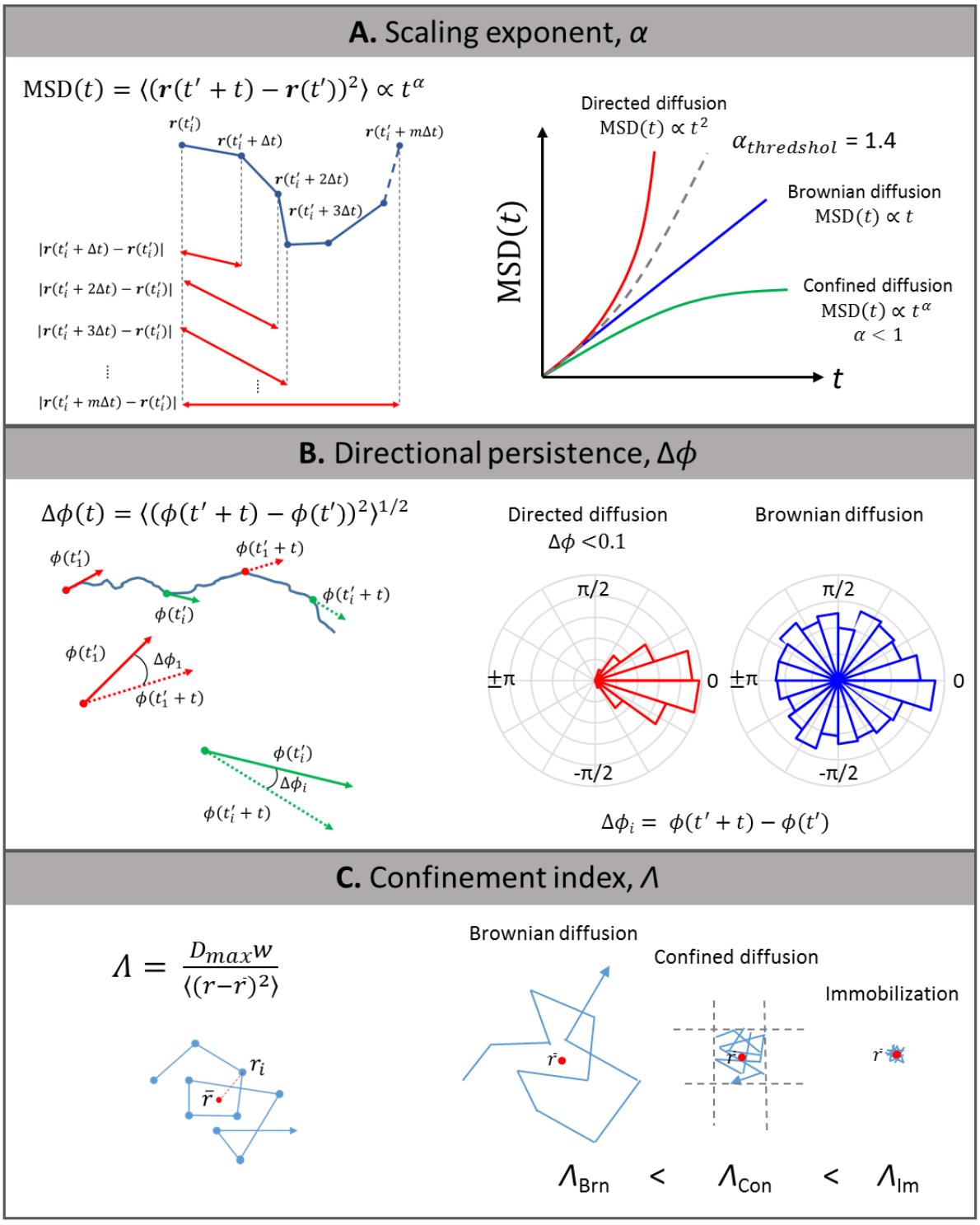

Figure S3 | Parameters for trajectory classification and segmentation

(A) Schematics show the calculation of a MSD curve and the representative MSD curves of directed diffusion, Brownian diffusion, and confined diffusion. **(B)** Schematics demonstrate the calculation of the directional persistence and the comparison of directional angles of directional diffusion and Brownian diffusion. **(C)** Calculation of confinement index and the indices derived from there three types of diffusions.

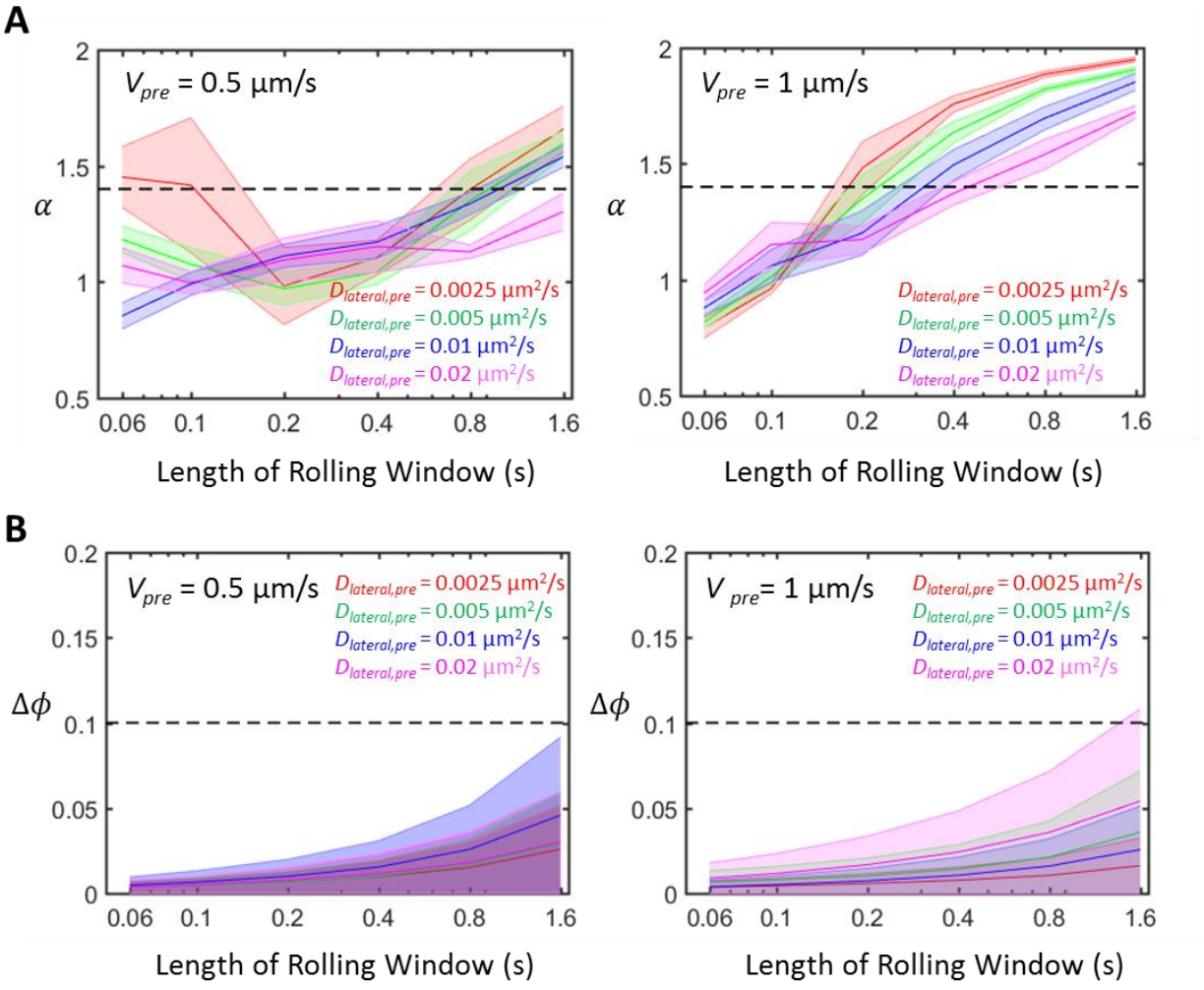

Figure S4 | Selecting threshold of the scaling exponent (α), directional persistence ($\Delta\phi$) and length of the rolling window (w) for directed diffusion detection (SME results)

Directed motions with various lateral diffusion coefficients (0.0025, 0.005, 0.01, or 0.02 μm²/s) and velocities (0.5 or 1 μm/s) were conducted in SME. The track duration for each trajectory is 10 seconds, and the time step is 2.5 ms. The α and $\Delta\phi$ values were derived from the MSD curves of the SME trajectoires. **(A)** The results demonstrate the diffusion would conceal the identification of directed motions, and the accuray of the algorithm depends on the window sizeWe set the threshold of identifying directed motion to be 1.4, because the active transport along microtubules exhibits α values of range from 1.4 to 2 in the cytosol (8). The time window was chosen as 1.6 s to achieve sufficient discrimination of active transport states. **(B)** Considering the time window of 1.6 s chosen to calculate α values, we set the threshold of $\Delta\phi$ values to be 0.1. Error bars (represented by color ribbons) show standard deviations of 10 runs.

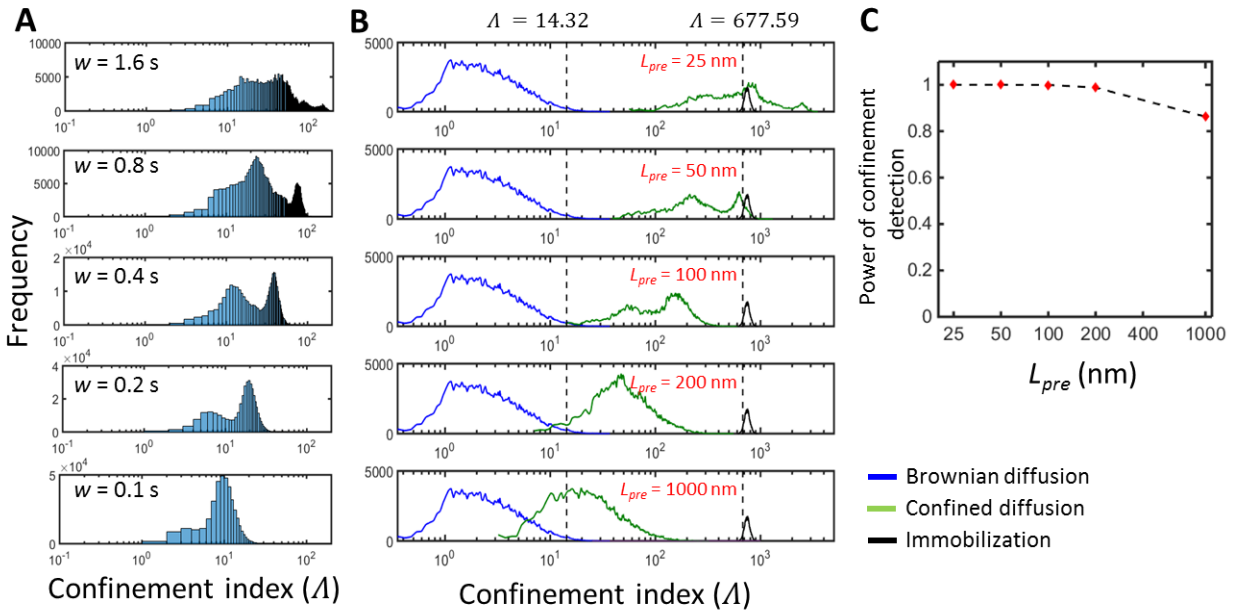

Figure S5 | Selecting thresholds of the confinement index Λ for confinement detection (Monte Carlo simulation results)

(A) The confinement index of Brownian motion is independent of the rolling window length (w) (15), but the confined index (Λ) of confined diffusion is a function of the rolling window length. **(B)** Histograms of confinement indices of freely diffusing particles (D_{Brn} = 0.08 μm^2/s, blue lines), particles diffusing within confinements of different sizes ($D_{micro,pre}$ = 0.08 μm^2/s and L_{pre} = 25, 50, 100, 200, and 1000 nm, green lines) and immobilized particles ($D = D_{min} = 4\times10^{-4}$ μm^2/s, black lines). In this simulation, we created diffusion confinements of various linear dimensions (L_{pre} = 25, 50, 100, 200, and 1000 nm) and penetrable boundary conditions (which mimic actin-cytoskeleton associated barriers and anchors). The particle can freely diffuse within the confinement ($D_{micro,\text{pre}}$ = 0.08 μm^2/s), with a probability of penetration P = 0.01 at the boundaries. We found the Λ threshod value of 14.32 can adequately differentiate confined diffusion from Brownian diffusion and the Λ threshod value of 677.59 can adequately differentiate confined diffusion from immobilization, repectively. As a result, here we define confinement diffusion to be $14.32 < \Lambda \leq 677.59$, where $\Lambda \leq 14.32$ is Brownian diffusion and $\Lambda > 677.59$ is immobilization. With this set of criteria, only 5% of simulated Brownian diffusion and immobilized trajectories were misclassified as confined diffusion. Our simulation results also indicated that the measured confinement index is a function of confinement size itself. As shown here, the set of criteria worked relatively well when the linear dimension of confinement is about 50-200 nm. The diameters of actin-induced compartments within plasma membrane range from 40 to 300 nm (5). **(C)** This plot shows that the power of distinguishing confined diffusion from Brownian diffusion. The Λ threshod value of 14.32 effectively separates confined diffusion from Brownian motion within the linear dimension of confinement (L_{pre}) below 200 nm (Power > 0.98). The statistical power is the probability that the test correctly differentiates trajectories of confined diffusion from those of Brownian diffusion.

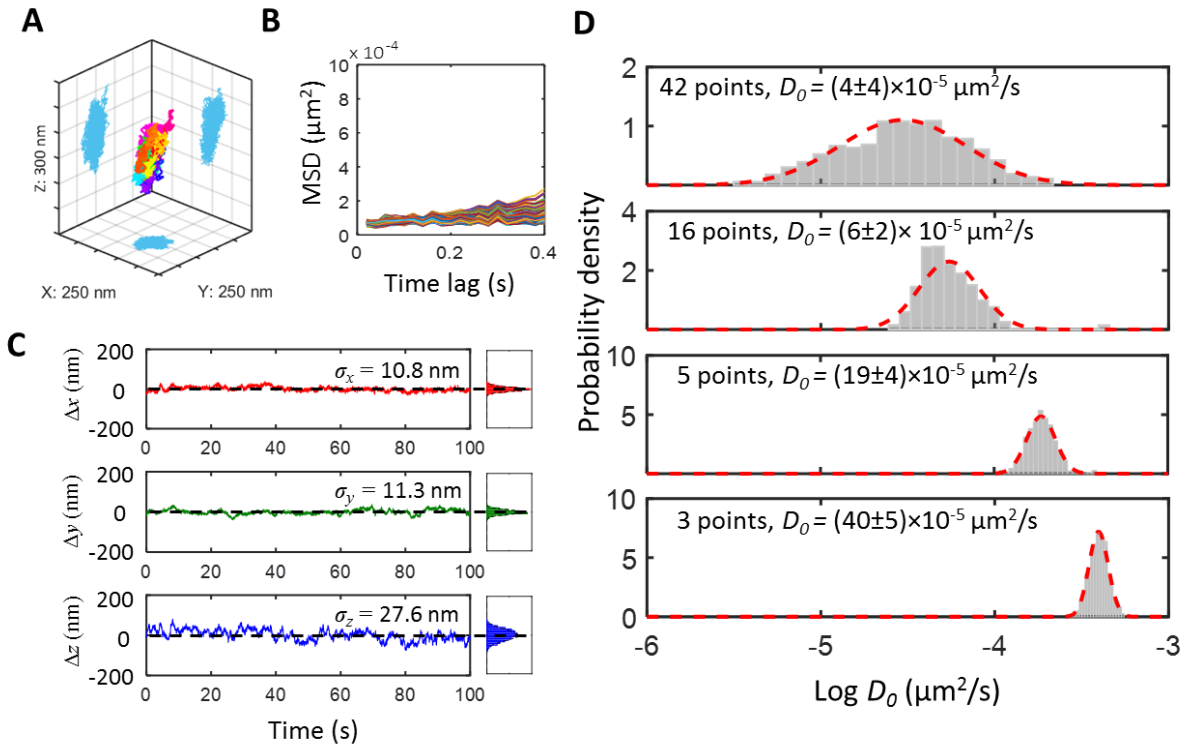

Figure S6 | Detection limit of TSUNAMI microscope (experimental tracking result)

To understand the lowest diffusion coefficient and the shortest linear dimension of confinement that TSUNAMI microscope can resolve, we performed tracking of fluorescent beads (⌀40 nm, Cat. No. F8770, Thermo Fisher Scientific) fixed in a 1.3% agarose matrix. The laser power was adjusted to achieve a photon count rate comparable to that of a real live cell tracking experiment (~400 kHz). **(A)** Representative trajectory of a bead immobilized in argarose matrix. **(B)** Segmented MSD curves using the rolling window of 1.6 s (w). The time step is 20 ms (Δt) and the sliding time step is 0.1 s (Δs). **(C)** Static tracking errors recored for x, y, and z dimesions respectively. The distances between each position (x_i, y_i, z_i) to the mean postion ($\bar{x}, \bar{y}, \bar{z}$) are Δx, Δy, and Δz. The static tracking errors, σ_x, σ_y, and σ_x, are the standard deviations of Δx, Δy, and Δz. Considering the "dynamic error" (i.e. tracking error) of the TSUNAMI microscope, the "static error" (due to the microscope thermomechanial instability) is estimated to be ~10 nm in x/y and 30 nm in z for 100-second-long experiments. **(D)** The finite values extracted from the MSD of immobilized bead represent the detection limit of the TSUNAMI system. To understand the how the number of MSD points affects the estimation of diffusion coefficients, the D_0 was estimated by fitting a MSD curve with a linear regreassion line using the first 3, 5, 16, or 42 MSD points. The number of MSD points were determined using a covariance-based estimator (19) with these following parameters: 10 nm tracking error in xy, 20 ms time step, 1.6 s tracking duration, 10^{-2}, 10^{-3}, 10^{-4}, or 10^{-5} μm²/s estimated diffusion coefficients, respectively. The D_0 converges with more MSD points, however, more MSD points also increase the variation of D_0. The number of MSD points used to estimate diffusivity of EGFRs is 3-5 points, so the lower bound of D_0 was defined as $D_0 = (19 \pm 4) \times 10^{-5}$ μm²/s using the first 5 MSD points.

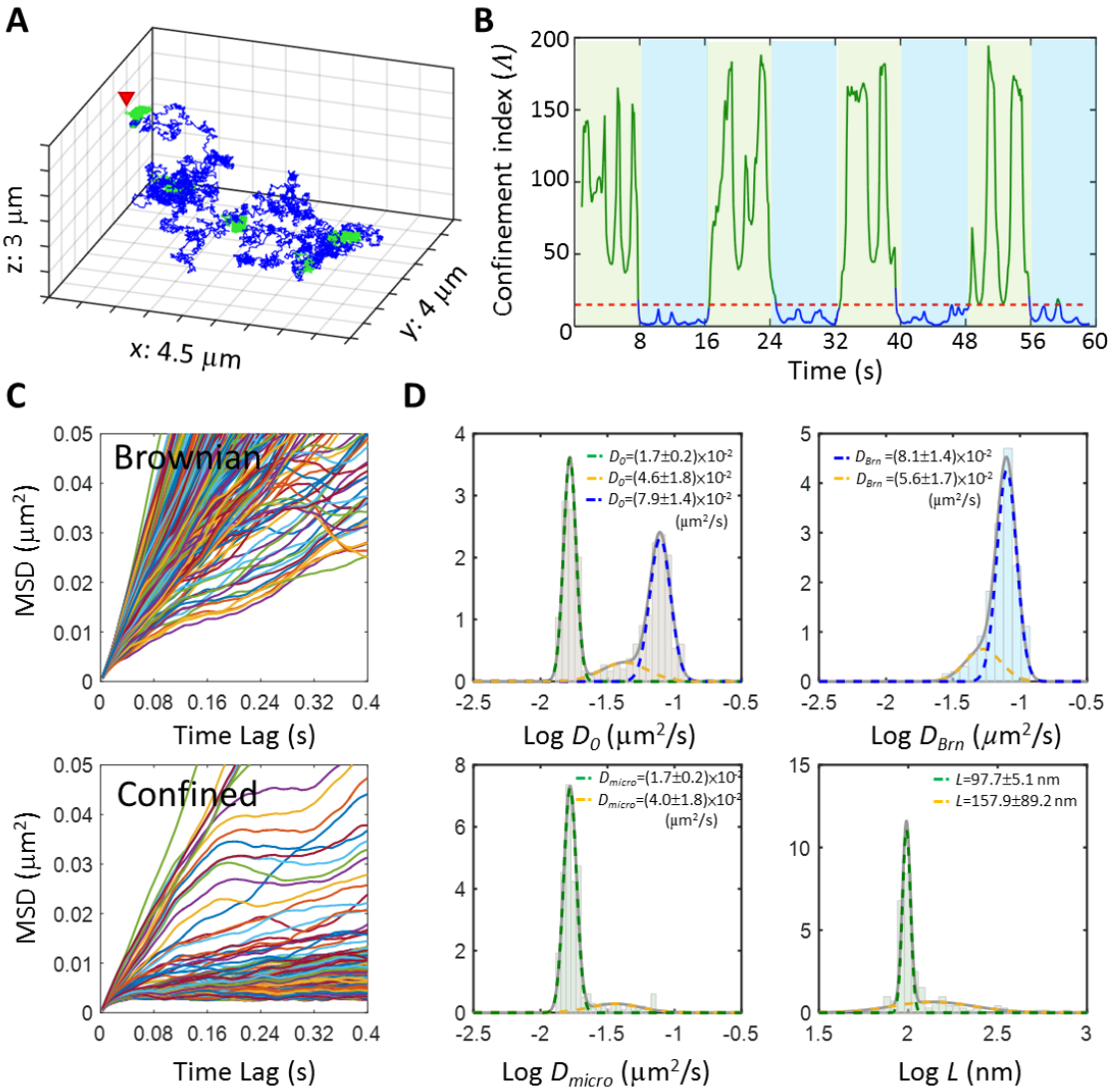

Figure S7 | Testing of MSD analysis and confinement detection (SME results)

(A) A Simulated trajectory composed of segments exhibiting Brownian diffusion and confined diffusion alternatively. Simulated condition: D_{pre} = 0.08 μm²/s, the linear dimension of confinements L_{pre} = 100 nm, probability of penetration P = 0.01 at the boundaries. The 64 s long trajectory is constituted of 8 segmemts exhibiting Brownian diffusion and confined diffusion (hop diffusion) by truns. Their motion patterns are determined by MSD analysis and confinement detection, and the trajectory are color-coded with either blue or green colors indicating Brownian diffusion and confined diffusion, respectively. The red arrow head indicates the starting point of the trajectory. **(B)** Profile of confinement index (Λ) of the trajectory. **(C)** MSD plots of segments classfied into Brownian diffusion (upper plot) or confined diffusion (lower plot). **(D)** Histograms of recovered diffusion coefficients, lengths of confined regions from Brownian diffusion (blue) or confined diffusion trajectories (green). The histograms were then fitted with a Gaussian mixture model. The fitted means and standard deviations were shown in the plots. D_{Brn} represents the recovered diffusion coefficient of Brownian trajectories. D_{micro} represents the recovered short-term diffusion coefficient of confined diffusion trajectories and D_{macro} is the recovered long-term diffusion coefficient extracted from the same trajectories. L is the recovered linear dimension of confinements.

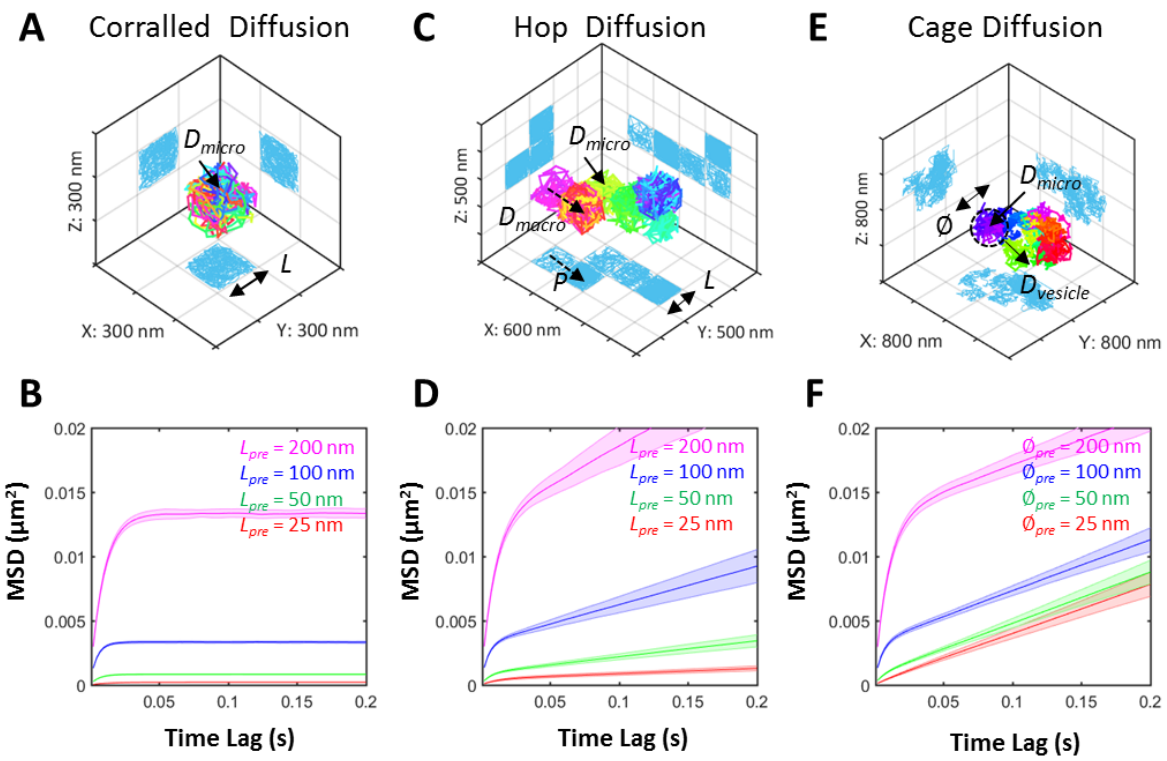

Figure S8 | MSD curves of simulation models (Monte Carlo simulation results)

MSD analysis on three types of confined diffusion models: corralled diffusion, hop diffusion and cage diffusion, which represent the possible motion patterns of EGFR trafficking. The stalled EGFRs in plasma membrane exhibits corralled diffusion (2). The hop diffusion represents the diffusion of EGFRs between membrane compartments (2, 20). The internalized EGFRs may demonstrate cage diffusion within endocytotic vesicles (13). We may be able to reveal the motion signatures of these three confined diffusion models using the MSD analysis. **(A)** Simulated corralled diffusion represents 3D isotropic diffusion in a meshwork of impenetrable barriers. **(B)** MSD plot starts linear and then reaches a plateau which identifies the confinement area and the corresponding length, L. The diffusion coefficient of this simulated confined diffusion is $D_{micro,pre}$ = 0.5 μm^2/s. **(C)** Simulated hop diffusion represents 3D isotropic diffusion in a meshwork of penetrable barriers. The prescribed length of square confinement area is L_{pre} and particles have a probability (P) of penetrating the barriers in every attempt to across barriers. **(D)** The slope of the MSD curve in long timescale is related to D_{macro}, and the meshwork constraints particle diffusion. The D_{micro} of freely diffusing particle in compartments is $D_{micro,pre}$ = 0.5 μm^2/s and the penetrating probability, P = 0.01. **(E)** Simulated cage diffusion represents freely diffusing particle ($D_{micro,pre}$ = 0.5 μm^2/s) restricted to a limited vesicle that itself can diffuse (the diffusion coefficient of the vesicle is $D_{vesicle,pre}$ = 0.01 μm^2/s and its diameter is $Ø_{pre}$ = 25 to 200 nm). **(F)** The slope of the MSD curve in short timescale is related to $D_{micro,}$ and the slope in long timescale depends on $D_{vesicle}$. Error bars (represented by color ribbons) show standard deviations of 100 runs.

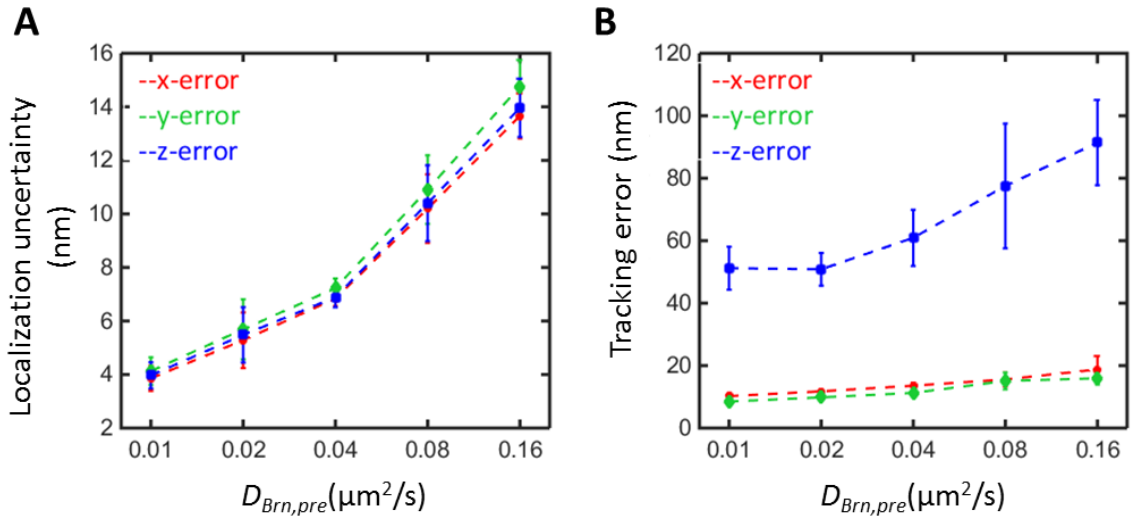

Figure S9 | Localization uncertainty of the xyz piezo stage and tracking error of TSUNAMI microscope are both related to the diffusivity of the particle (SME results)

(A) The localization uncertainty of the xyz piezo stage is defined as the standard deviation of the difference between the Monte-Carlo-simulation-generated trajectory that is used to command the movement of the xyz piezo stage and the actual trajectory that the stage performs (output from the capacitance sensors in the xyz piezo stage). The stage localization uncertainty increases with increasing diffusion coefficient in the SME. **(B)** The tracking error of TSUNAMI microscope is defined as the standard deviation of the difference between the stage trajectory (output from the capacitance sensors in the xyz piezo stage) and the TSUNAMI tracking trajectory. The tracking error was less than 20 nm in x and y and ranged from 50.8 nm to 91.4 nm in z, depending on the diffusivities used in the SME. Error bars show standard deviations of 10 runs.

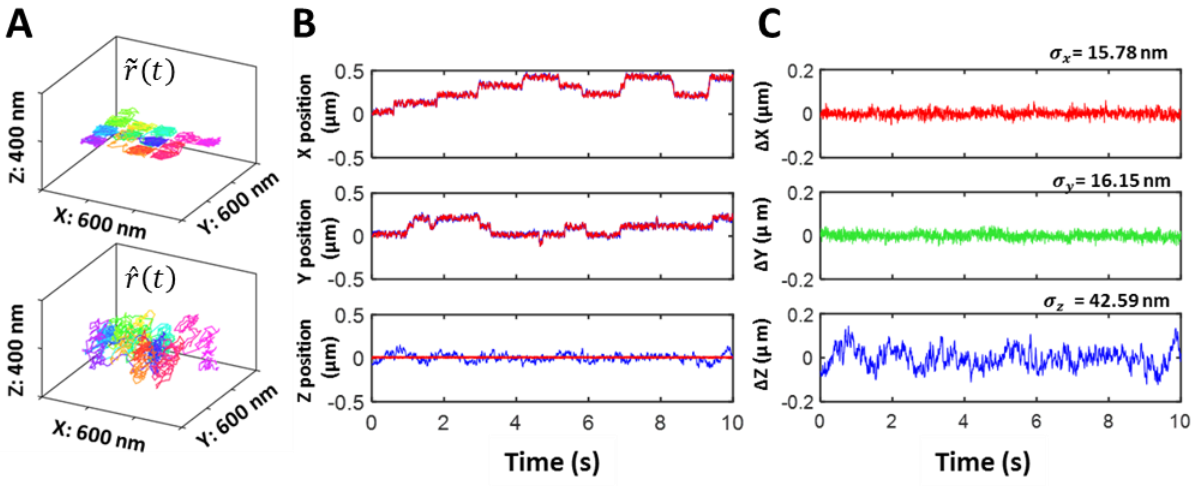

Figure S10 | TSUNAMI tracking error in 2D confined diffusion (SME results)
(A) The tracer was driven by an independent xyz piezo stage along the prescribed trajectories mimicking various motions, and the stage trajectory and the tracking trajectory were read from the piezo stage and TSUNAMI microscope. **(B)** The one-dimensional trajectories in x, y, z. The red line represents the stage trajectories and the blue ones are from tracking trajectories. **(C)** Comparing these two trajectories, the tracking errors in x, y, z directions were evaluated. The prescribed trajectory was simulated from a 2D confined diffusion model with diffusion coefficient D = 0.5 μm^2/s, probability of penetration P = 0.01 at the boundaries, and length of square compartment L = 100 nm.

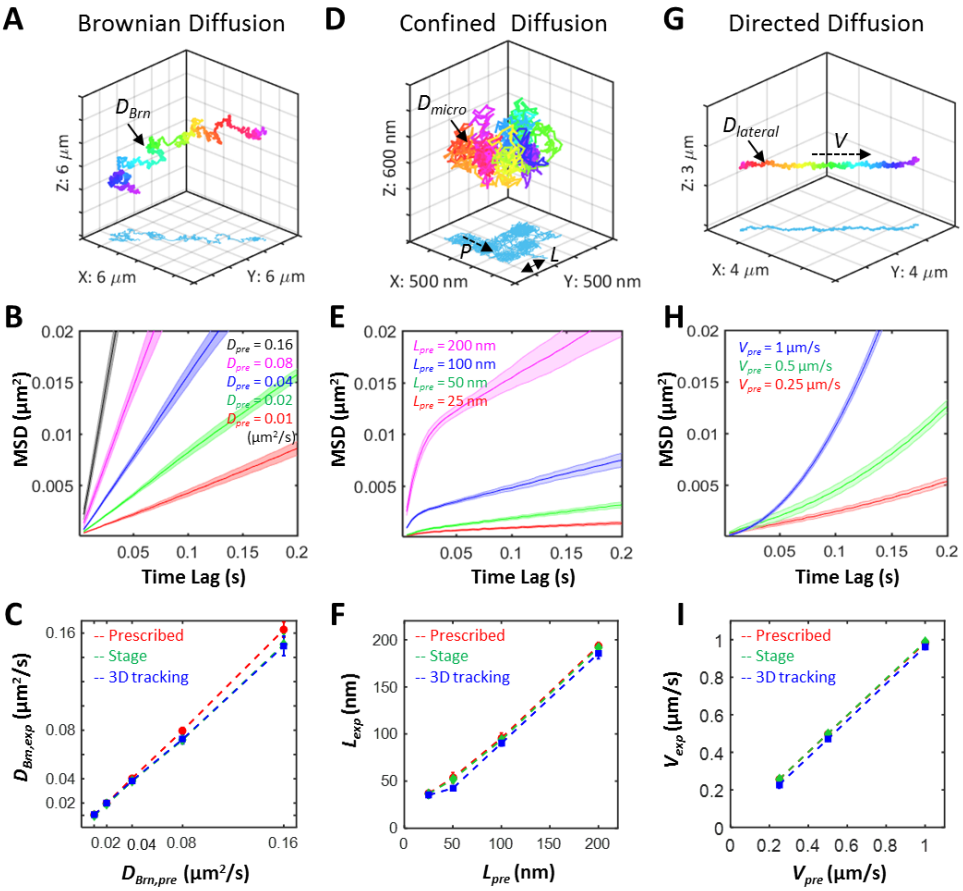

Figure S11 | MSD analysis on Brownian, confined and directed diffusion (SME results)
These SME results demonstrate that the TSUNAMI microscope is able to follow the trajectories of all three types of predefined motions (Brownian, confined, and directed diffusion), and our MSD analysis algorithm is capable of recovering the physical parameters (D_{Brn}, L and V) encoded in the prescribed trajectories. **(A)** A representative 3D tracking trajectory of Brownian diffusion with diffusivity D_{Brn} = 0.08 μm²/s. **(B)** For Brownian diffusion, the resulting MSD curves are linear with an increasing slope for larger diffusivity. **(C)** The experimental diffusivities recovered from the MSD analysis (D_{Brn}) match well with the values encoded in the prescribed trajectories (D_{pre}). R-squared values of fitted MSD curves are all above 0.99. goodness-of-fit of the fitted MSD curves was**(D)** A representative 3D tracking trajectory of confined diffusion with diffusivity D = 0.5 μm²/s in confinements of linear dimension L = 100 nm. The particle has the probability of penetration P = 0.01 at the boundaries. **(E)** For confined diffusion, the resulting MSD curves are linear initially (with a slope depends on D_{micro}) and then deviates toward a lower slope value (so-called subdiffusion). **(F)** The experimental linear dimensions of confinements recovered from the MSD analysis (L_{exp}) match well with the values encoded in the prescribed trajectories (L_{pre}). **(G)** A representative 3D tracking trajectory of directed diffusion with active transport speed V = 0.5 μm/s and lateral diffusivity $D_{lateral}$ = 0.0025 μm²/s. **(H)** For directed diffusion, the resulting MSD curves exhibit increasing slope at longer time lag (so-called superdiffusion), with the scaling exponent α = 2 for pure directed transport. Increasing lateral diffusivity in directed diffusion reduces the scaling exponent. **(I)** The experimental transport speeds recovered from the MSD analysis (V_{exp}) match well with the values encoded in the prescribed trajectories (V_{pre}). Error bars and ribbons represent standard deviations from 10 runs for each condition.

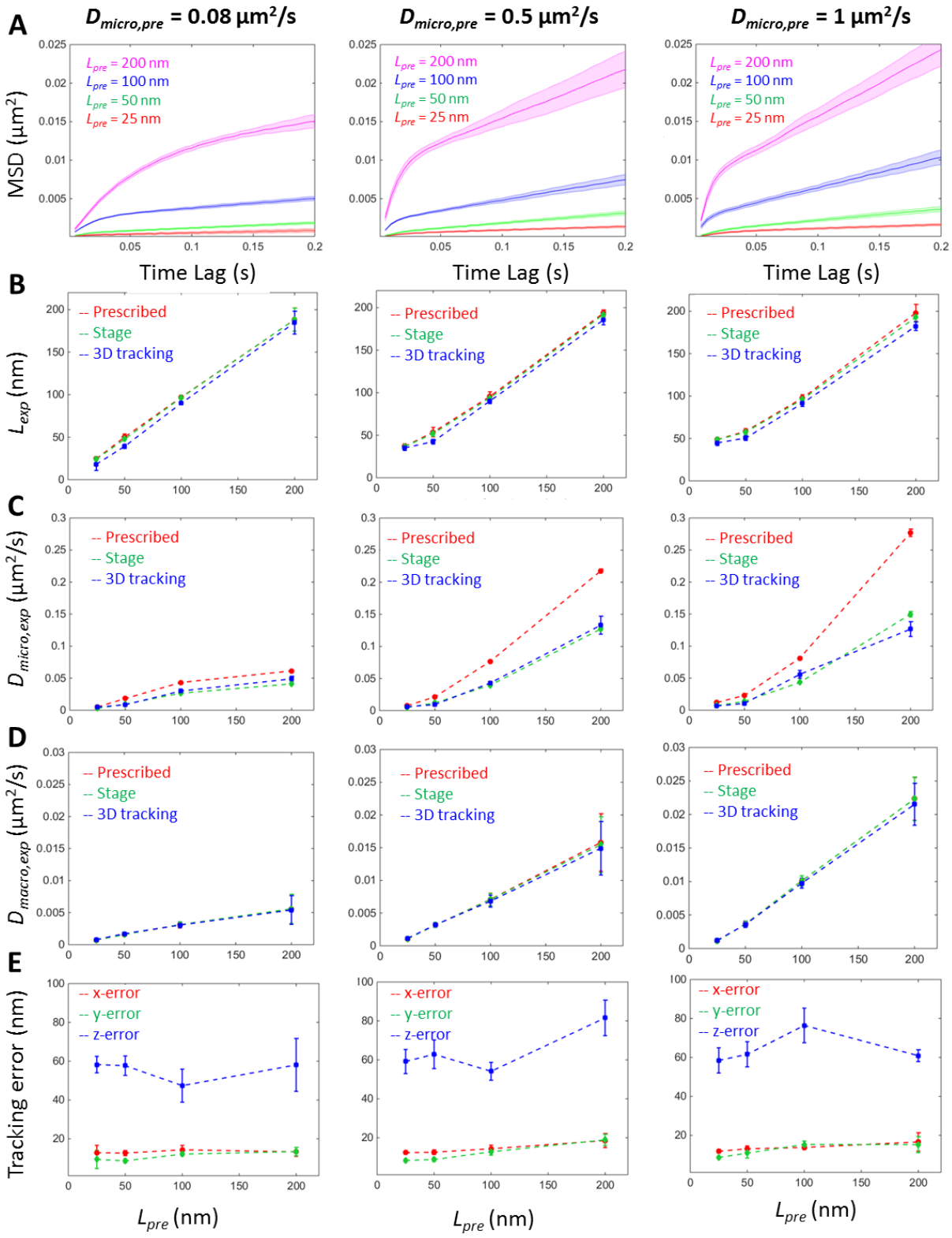
A
$D_{micro,pre}$ = 0.08 μm²/s
$D_{micro,pre}$ = 0.5 μm²/s
$D_{micro,pre}$ = 1 μm²/s
MSD (μm²)
L_{pre} = 200 nm
L_{pre} = 100 nm
L_{pre} = 50 nm
L_{pre} = 25 nm
Time Lag (s)
B
L_{exp} (nm)
C
$D_{micro,exp}$ (μm²/s)
D
$D_{macro,exp}$ (μm²/s)
-- Prescribed
-- Stage
-- 3D tracking
E
Tracking error (nm)
-- x-error
-- y-error
-- z-error
L_{pre} (nm)

F R^2 values for MSD curve fitting

D (μm²/s) \ *L* (nm)	25	50	100	200
0.08	0.738±0.117	0.957±0.007	0.994±0.004	0.995±0.008
0.5	0.908±0.024	0.979±0.007	0.999±0.001	0.998±0.001
1	0.951±0.019	0.993±0.003	0.986±0.016	0.990±0.003

Figure S12 | More MSD analysis on confined diffusion (SME results)

We further tested our MSD analysis algorithm using the confined diffusion with various D_{micro} and L values encoded in the simulated trajecotries used for SME. The particle had the probability of penetration $P = 0.01$ at the boundaries. This thorough examination further validates the reliablity of our MSD analysis algorithm in extracting encoded dynamic parameters (L and D_{micro}) and the fidelity of TSUNAMI microscope in tracking single particles under physiologically relevant conditions. **(A)** As expected, the resulting MSD curves show the signature of subdiffusion. **(B)** The experimental linear dimensions of confinements recovered from the MSD analysis (L_{exp}) match well with the values encoded in the predefined trajectories (L_{pre}) at all three diffusivities. **(C)** The short-term microscopic diffusivity, D_{micro}, obtained from the MSD analysis is influenced by the confinement size. Here we show that the short-term microscopic diffusivity D_{micro} estimated from the confined diffusion model (Equations 6 and 7) is a function of confinement size, and this finding agrees with the research of Salome's group. (21). D_{micro} is approaching the encoded value of 0.08 μm²/s only when the confinement size is sufficiently large. This result is in agreement with other research. Eggeling's group has reported that the cortical actin cytoskeleotn compartmentalised phospholipid diffusion and reduced the diffusivity of phospholipid (22). **(D)** The long-term macroscopic diffusivity, D_{macro}, obtained from the MSD analysis is also influenced by the confinement size. **(E)** Tracking error is quantified by the standard deviations of the difference between the stage trajectory (output from the capacitance sensor in the xyz piezo stage) and the TSUNAMI tracking trajectory. The tracking errors shown here are consistent with our previous observation. Error bars and ribbons represent standard deviations from 10 runs for each condition. **(F)** The goodness-of-fit of MSD curve fitting with Equation 6 (confined diffusion, in main text) was evaluated by R-squared measurment.

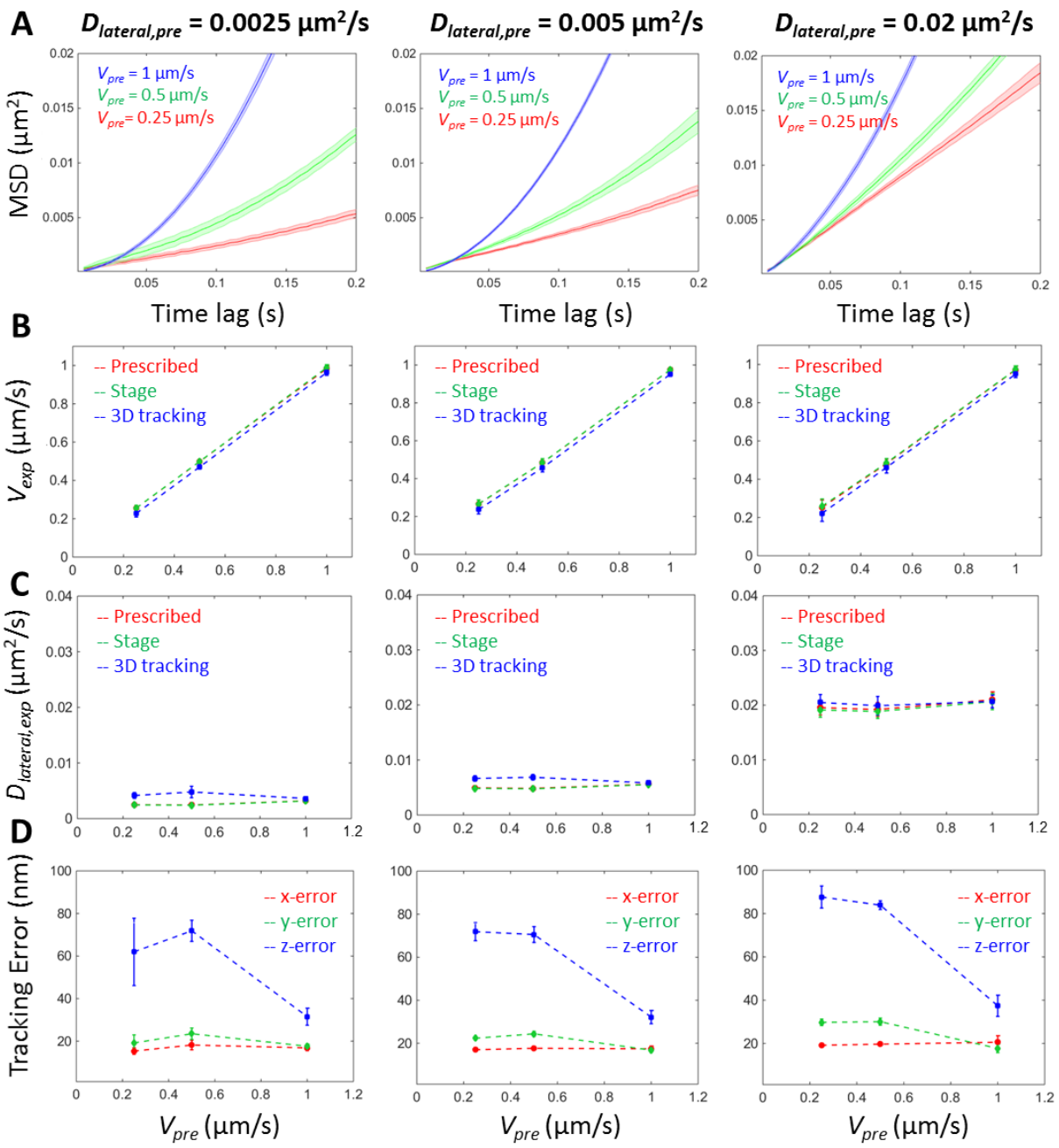

E R^2 values for MSD curve fitting

D_{Lat} (µm²/s) \ V (µm/s)	0.25	0.5	1
0.0025	0.946±0.016	0.968±0.006	0.984±0.010
0.005	0.973±0.004	0.987±0.002	0.980±0.009
0.02	0.999±0.001	0.997±0.001	0.979±0.010

Figure S13 | More MSD analysis on directed diffusion (SME results)

We further tested our MSD analysis algorithm using the directed diffusion with various D and V values encoded in the simulated trajecotries used for SME. **(A)** The MSD curves grow with time lag, exhibiting the signature of super-diffusion. The scaling exponent α is approaching 2 when the diffusivity D is vanishing. However, if D is large, the random motion would mask the directed transport. **(B)** The V_{exp} values extracted from the MSD analysis match well with the encoded V values. **(C)** The D_{exp} values extracted from the MSD analysis match well with the encoded D values at all three transport speeds. **(D)** Tracking error is quantified by the standard deviation of the difference between the stage trajectory (output from the capacitance sensor in the xyz piezo stage) and TSUNAMI tracking trajectory. The tracking error results shown here are consistent with our previous observation. Error bars and ribbons represent standard deviations from 10 runs for each condition. **(E)** The goodness-of-fit of MSD curve fitting with Equation 5 (directed diffusion, in main text) was evaluated by R-squared measurment.

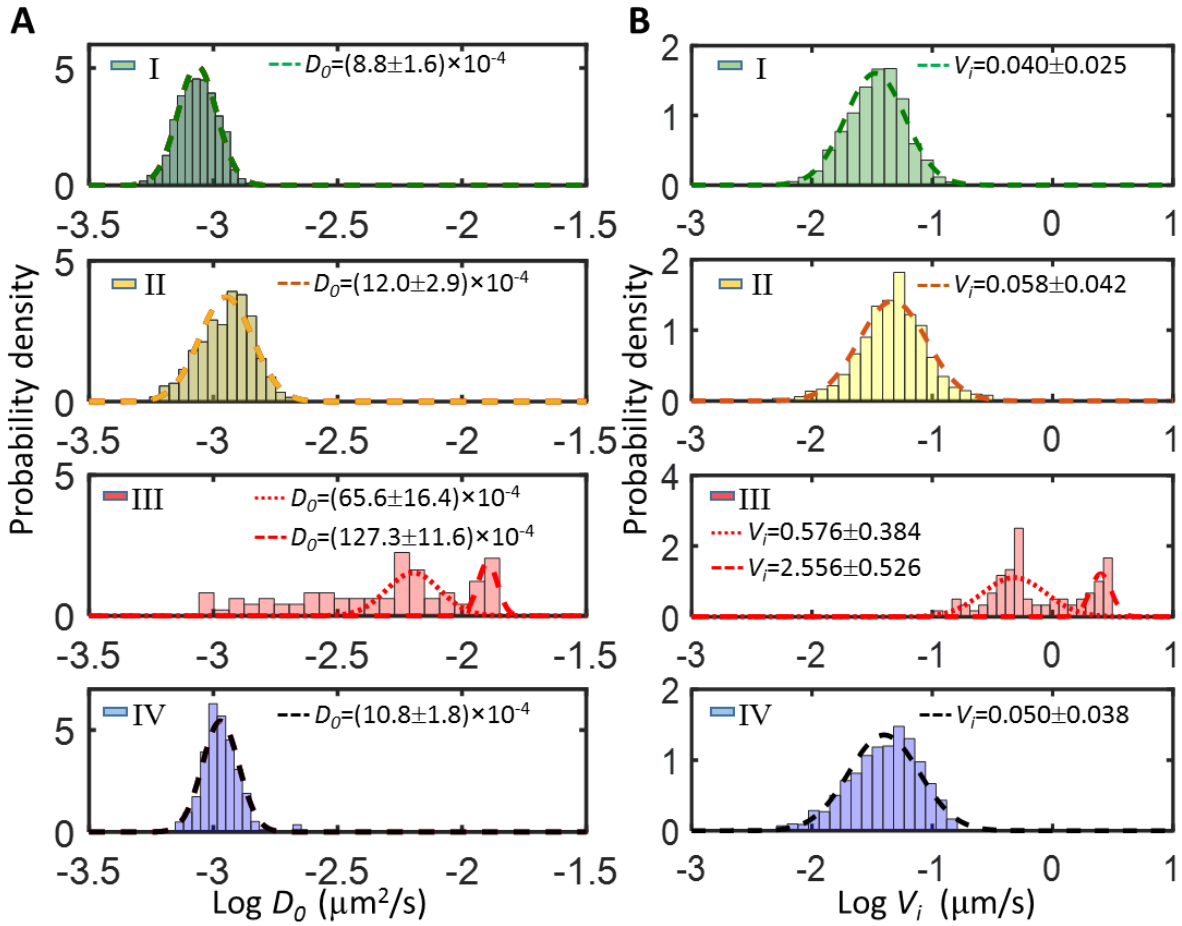

Figure S14 | Dynamic parameters of the EGFR in these four phases

Histograms of log D_o **(A)** and log V_i **(B)** in four phases of a 442-second-long trajectory (shown in Figure 5 of main text). This trajectory was dissected using the algorithm of segmentation and classification. The classified and color-coded trajectory provides a reliable guidance to identify the motional patterns of EGFRs in various phases, such as diffusion on the cell membrane, endocytosis, and active transport in cytoplasm. The dynamic parameters extracted from different phases could be used to characterized the motional features of EGFR trafficking. The diffusion coefficients (D_0) and the instantaneous velocities (V_i) recovered from the segmented trajectories of Phase III significantly differentiate from those parameters of the other three phases. As shown in the plots, the increase of instantaneous velocities is also correlated with the increase of diffusion coefficients.

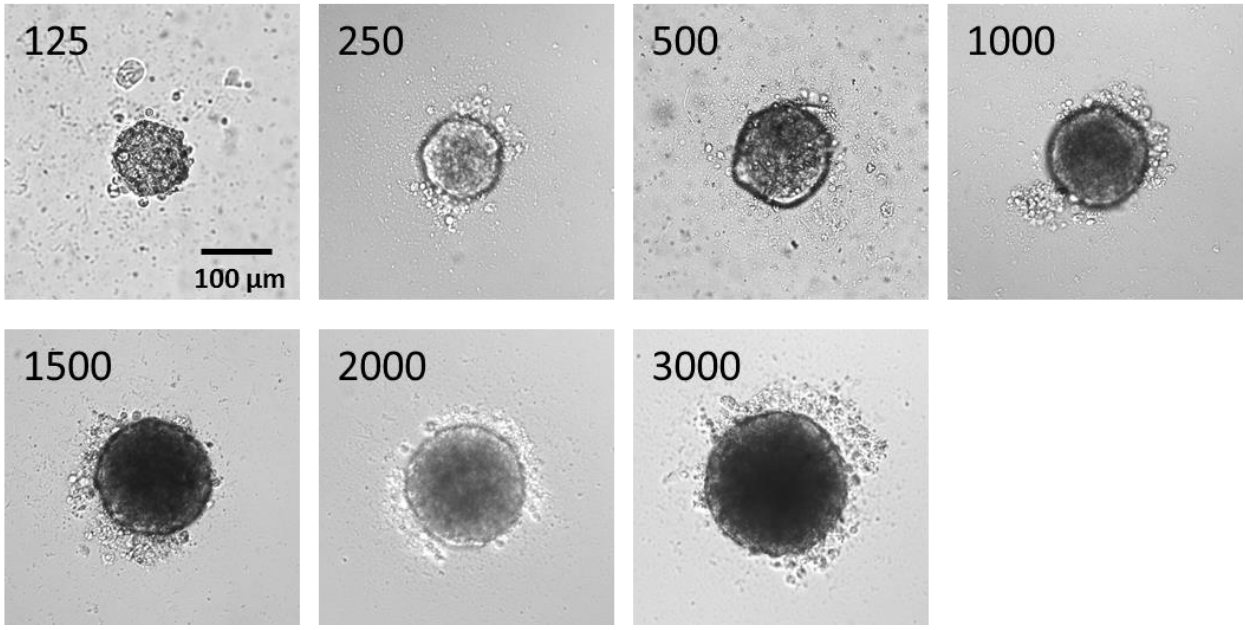

Figure S15 | Spheroid formation

Bright field imaging of multicellular cancer spheroids formed in liquid overlay from dissociated, exponentially growing A431 skin epidermoid carcinoma cells after a 96-hr initiation interval in agarose-coated 96-well microliter plates. The seeding density was between 125 and 3000 per well in 200 µl of serum-conditioned high glucose standard medium. The concentration to routinely and reproducibly obtain spheroids with a diameter of 90-110 µm is 125 cells per well. Scale bar is 100 µm. The preparation of multicellular spheroids was based on the method developed by Kunz-Schughart's group. (23)

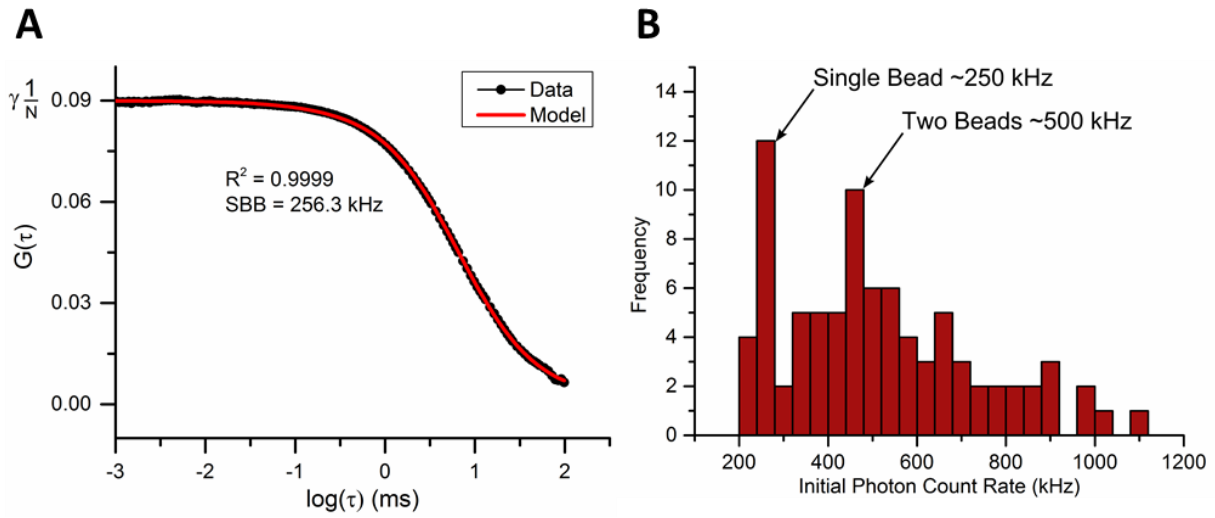

Figure S16 | Characterization of fluorescent beads for 3D tracking

(**A)** FCS Experiments and (**B)** TSUNAMI tracking trajectory analysis were used to characterize the single -bead brightness (SBB) and to estimate the number of beads attached to EGFR molecules during live cell experiments. FCS was performed with ⌀40 nm fluorescent microspheres (F8770, Thermo Fisher Scientific) in 16 nM concentration with a single excitation beam at 3 mW average power. Laser power and detector gain settings were matched to live cell experimental conditions. Raw photon counts were auto-correlated in real-time using a digital correlator (7002/USB, ALV). Autocorrelation curves (black dots) were averaged from 20 runs of 10 seconds each. Further verification of SBB is done by analyzing 95 individual trajectories' count rates. **(B)** Histogram of trajectory count rates at early time points in a fixed sample of ⌀40 nm fluorescent beads suspended in agarose. The initial count rate was taken to be the first 5 seconds of the trajectory after the controller had stably locked onto the particle (~100 ms). The histogram uncovers two peaks of brightness surrounded by a wide distribution ranging from 200 kHz to 1.1 MHz. The first peak is most likely the single bead brightness of 255 kHz whereas the second peak, at ~500 kHz, is likely a dimer. In our experiments, we made sure that we were following a single bead, not a two-bead system. This characterization has been done and published in *Nature Communications* (17), and more detailed discussion please see the supplementary information of the *Nature Communications* article.

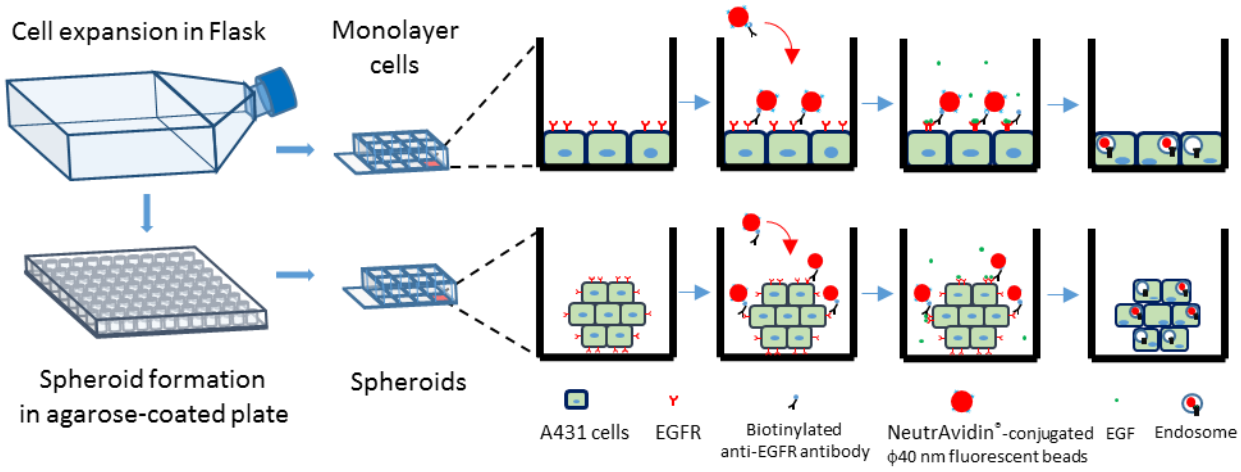

Figure S17 | Preparation of samples for EGFR tracking

A431 cells were expanded in flasks and the dissociated into single-cell suspension with trypsin treatment. For EGFR tracking on monolayer cells, the cells from suspension were directly seeded into chambered coverglasses and incubated for 24-48 hr. After 24-hr serum starvation, the monolayer cells were stained with CellMask™ Deep Red and their EGFRs were recognized by monoclonal anti-EGFR IgG conjugated ϕ 40 nm fluorescent nanoparticles. For spheroids, the suspended single cells were seeded into agarose-coated and incubated for 96 hours to form spheroids. Both monolayer cells and spheroids were treated with serum starvation 24 hour before EGFR tracking. The spheroids were then transferred to chambered coverglasses for membrane staining and EGFR labeling.

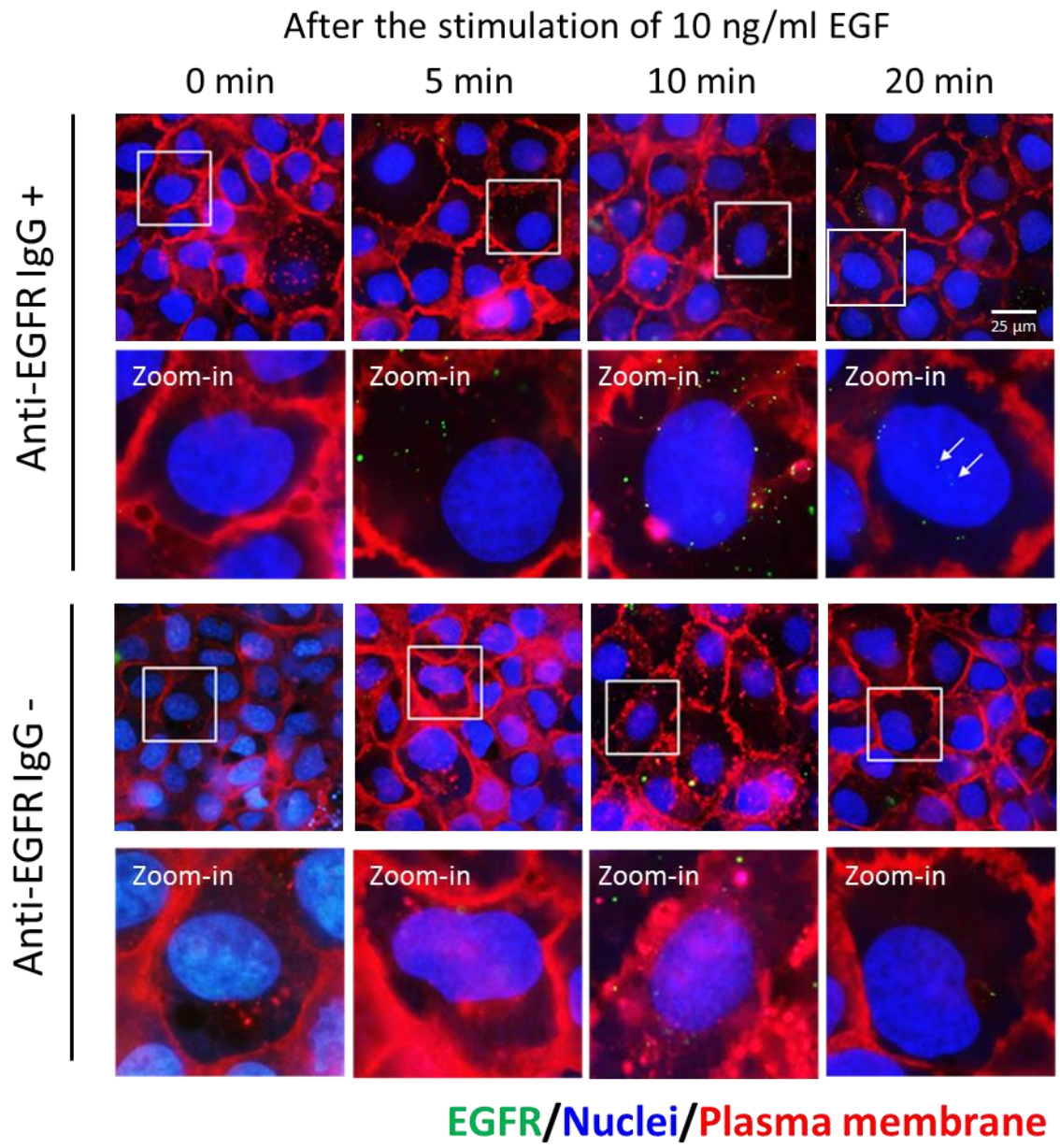

Figure S18 | EGF induces internalization of EGFR

Monolayer A431 cells were exposed to serum-free media overnight, and then their EGFRs were tagged with biotin-conjugated anti-EGFR antibodies, and NeutrAvidin® conjugated red FluoSpheres® (F8770, Thermo Fisher Scientific) bound to biotins to label EGFRs. In control group, we didn't label EGFR with anti-EGFR antibodies. After labeling, cells were treated with EGF (10 ng/ml) for indicated time. The white arrows indicate nuclear translocation of EGFR. The boxed areas are shown in detail in the zoom-in. Scale bar is 25 μm.

Supplementary References

1. Low-Nam, S. T., K. A. Lidke, P. J. Cutler, R. C. Roovers, P. M. v. B. en Henegouwen, B. S. Wilson, and D. S. Lidke. 2011. ErbB1 dimerization is promoted by domain co-confinement and stabilized by ligand binding. Nature structural & molecular biology 18:1244-1249.
2. Clausen, M. P., and B. C. Lagerholm. 2013. Visualization of plasma membrane compartmentalization by high-speed quantum dot tracking. Nano letters 13:2332-2337.
3. Kusumi, A., Y. Sako, and M. Yamamoto. 1993. Confined lateral diffusion of membrane receptors as studied by single particle tracking (nanovid microscopy). Effects of calcium-induced differentiation in cultured epithelial cells. Biophysical journal 65:2021-2040.
4. Morone, N., T. Fujiwara, K. Murase, R. S. Kasai, H. Ike, S. Yuasa, J. Usukura, and A. Kusumi. 2006. Three-dimensional reconstruction of the membrane skeleton at the plasma membrane interface by electron tomography. The Journal of cell biology 174:851-862.
5. Kusumi, A., T. A. Tsunoyama, K. M. Hirosawa, R. S. Kasai, and T. K. Fujiwara. 2014. Tracking single molecules at work in living cells. Nature chemical biology 10:524-532.
6. de Bruin, K., N. Ruthardt, K. von Gersdorff, R. Bausinger, E. Wagner, M. Ogris, and C. Bräuchle. 2007. Cellular dynamics of EGF receptor–targeted synthetic viruses. Molecular Therapy 15:1297-1305.
7. Ruthardt, N., D. C. Lamb, and C. Bräuchle. 2011. Single-particle tracking as a quantitative microscopy-based approach to unravel cell entry mechanisms of viruses and pharmaceutical nanoparticles. Molecular Therapy 19:1199-1211.
8. Fakhri, N., A. D. Wessel, C. Willms, M. Pasquali, D. R. Klopfenstein, F. C. MacKintosh, and C. F. Schmidt. 2014. High-resolution mapping of intracellular fluctuations using carbon nanotubes. Science 344:1031-1035.
9. Saxton, M. J. 1997. Single-particle tracking: the distribution of diffusion coefficients. Biophysical journal 72:1744.
10. Wade, W. F., J. H. Freed, and M. Edidin. 1989. Translational Diffusion of Class-Ii Major Histocompatibility Complex-Molecules Is Constrained by Their Cytoplasmic Domains. Journal of Cell Biology 109:3325-3331.
11. Burmaster, D. E., and D. A. Hull. 1997. Using Lognormal distributions and Lognormal probability plots in probabilistic risk assessments. Hum Ecol Risk Assess 3:235-255.
12. Lin, C., M. Schuster, S. C. Guimaraes, P. Ashwin, M. Schrader, J. Metz, C. Hacker, S. J. Gurr, and G. Steinberg. 2016. Active diffusion and microtubule-based transport oppose myosin forces to position organelles in cells. Nature communications 7.
13. Huet, S., E. Karatekin, V. S. Tran, I. Fanget, S. Cribier, and J.-P. Henry. 2006. Analysis of transient behavior in complex trajectories: application to secretory vesicle dynamics. Biophysical journal 91:3542-3559.
14. Jin, H., D. A. Heller, and M. S. Strano. 2008. Single-particle tracking of endocytosis and exocytosis of single-walled carbon nanotubes in NIH-3T3 cells. Nano Letters 8:1577-1585.
15. Meilhac, N., L. Le Guyader, L. Salome, and N. Destainville. 2006. Detection of confinement and jumps in single-molecule membrane trajectories. Physical Review E 73:011915.
16. Sergé, A., N. Bertaux, H. Rigneault, and D. Marguet. 2008. Dynamic multiple-target tracing to probe spatiotemporal cartography of cell membranes. Nature methods 5:687-694.
17. Perillo, E. P., Y.-L. Liu, K. Huynh, C. Liu, C.-K. Chou, M.-C. Hung, H.-C. Yeh, and A. K. Dunn. 2015. Deep and high-resolution three-dimensional tracking of single particles using nonlinear and multiplexed illumination. Nature communications 6.
18. Liu, C., Y.-L. Liu, E. Perillo, N. Jiang, A. Dunn, and H.-C. Yeh. 2015. Improving z-tracking accuracy in the two-photon single-particle tracking microscope. Applied physics letters 107:153701.

19. Vestergaard, C. L., P. C. Blainey, and H. Flyvbjerg. 2014. Optimal estimation of diffusion coefficients from single-particle trajectories. Physical Review E 89.
20. Clausen, M. P., E. C. Arnspang, B. Ballou, J. E. Bear, and B. C. Lagerholm. 2014. Simultaneous multi-species tracking in live cells with quantum dot conjugates. PloS one 9:e97671.
21. Daumas, F., N. Destainville, C. Millot, A. Lopez, D. Dean, and L. Salome. 2003. Confined diffusion without fences of a G-protein-coupled receptor as revealed by single particle tracking. Biophysical Journal 84:356-366.
22. Andrade, D. M., M. P. Clausen, J. Keller, V. Mueller, C. Wu, J. E. Bear, S. W. Hell, B. C. Lagerholm, and C. Eggeling. 2015. Cortical actin networks induce spatio-temporal confinement of phospholipids in the plasma membrane–a minimally invasive investigation by STED-FCS. Scientific reports 5.
23. Friedrich, J., C. Seidel, R. Ebner, and L. A. Kunz-Schughart. 2009. Spheroid-based drug screen: considerations and practical approach. Nature protocols 4:309-324.